Multi-Interface polarization engineering constructed 1T-2H MoS$_2$ QDs/Y-NaBi(MoO$_4$)$_2$ multiple heterostructure for high-efficient piezoelectric-photoelectrocatalysis PDE-5i degradation

Qing-rui Zeng [a,b,1], Zi-ang Jia [a,b,1], Xu Liu [a], Bo-wen Xiu [c], Jin-ping Cheng [a,b,*]

[a] School of Environmental Science and Engineering, Shanghai Jiao Tong University, Shanghai 200240, PR China
[b] State Environmental Protection Key Laboratory of Environmental Health Impact Assessment of Emerging Contaminants, School of Environmental Science and Engineering, Shanghai Jiao Tong University, Shanghai 200240, PR China
[c] School of Chemistry and Chemical Technology, Shanghai Jiao Tong University, Shanghai 200240, PR China

ABSTRACT

The rational application of piezoelectric polarization properties in non-centrosymmetric heterojunctions to improve charge separation efficiency is a novel approach for enhancing their photoelectrocatalytic capabilities for environmental purification. Herein, a noval 1T-2H MoS$_2$ QDs/Y-NaBi(MoO$_4$)$_2$ multiple heterostructures with two types S-scheme heterojunctions was formed by multi-functional materials NaBi(MoO$_4$)$_2$ with Y^{3+} ion-doping and multi-phase state (1T, 2H and 1T-2H) MoS$_2$ quantum dots multi-interface polarization engineering. Material characterization and DFT calculations revealed that 1T-2H MoS$_2$ QDs/Y-NaBi(MoO$_4$)$_2$ multiple heterostructures produce highly-efficient Bi-S-Mo(IV) and Mo(IV)-S-Mo(VI) charge-transfer channels induced by multi-interface polarization engineering. 1T-2H MoS$_2$ QDs/Y-NaBi(MoO$_4$)$_2$ heterostructures were developed as photoanodes using the pressed tablet stainless-steel mesh (PT-SSM) method, and demonstrated conspicuous piezoelectric-photoelectrocatalytic (PZ-PEC) efficiency (99.88% removal within 40 min) for the degradation of organic pollutant phosphodiesterase-5 inhibitor (PDE-5i) under visible light illumination, direct-current external bias and mechanical force. This work provides new insight for synergy and mechanism between piezoelectric effect and photoelectrocatalysis for environmental clean-up.

1. Introduction

Since the onset of the global COVID-19 pandemic, the industrial structures of many countries has been changed, resulting in countless new pollutants entering the natural environment and triggering new ecological collapse concerns. Phosphodiesterase-5 inhibitors (PDE-5i) have emerged as a new category of pollutant [1] with Sildenafil, Tadalafil, and Vardenafil is the primary sources [2,3]. Although PDE-5i was first developed to treat *altitude sickness*, *ischemic heart*, and *pulmonary hypertension*, it is currently best known as a treatment for *erectile dysfunction* [4–7]. Previous research has reported the side effects of PDE-5i abuse [8]. For instance, Sildenafil, the main component in PDE-5i with 70% content, which can cause chronic toxicity in *Daphnia* even below levels 0.64 mg·L^{-1}. Moreover, significant mutagenic and genotoxic potential begins to arise, when it is in the range of 2–15 mg·L^{-1} [9]. Sildenafil was predicted to have a total no-effect concentration of 640 ng·L^{-1} [10]. PDE-5i abuse already generates enormous strain on sewage treatment plants (STP), regardless of the average time and during the COVID-19 [11–15], and surveys have indicated that Tadalafil and Vardenafil are readily removed by STP, whereas Sildenafil is difficult to eliminate [1,12,14,16–18]. As the main component of PDE-5i, Sildenafil may pose high environmental risks, warranting further investigation. Unfortunately, conventional Advanced oxidation processes (AOP) methods, such as chlorination oxidation [9] and UV/O$_3$ oxidation [19] have difficulty degrading the macromolecular structure of Sildenafil,. Meanwhile, Sildenafil has extremely limited oxidative degradation capacity and can only slightly oxidize the zinc in the whole Sildenafil molecule *via* the chlorination oxidation method [9]. Even

when using the strong oxidation method UV/O$_3$, the Sildenafil molecular oxidation degradation with two types of annular structures undergoes minimal further degradation [19]. Moreover, one of the reasons for the difficulty in removing Sildenafil and Vardenafil is that they can be interchanged in the presence of sunlight [20].

Among the emerging AOPs techniques, photoelectrocatalysis (PEC) has attracted considerable attracts extensive attention for pollutant removal because of its benefits such as safe and mild reaction conditions, high reusability, no secondary pollution, and simplicity of commercialization. Among the fundamental photoelectrode materials, photoelectrocatalysts are the most critical components that determine the degradation efficiency of PEC [21–25]. Futhermore, piezoelectric effect may effectively regulate the formation and transport of electric charges through the internal electric field created by piezoelectric polarization [26,27], allowing piezoelectric materials to directly convert mechanical energy into chemical energy [27] for environmental purification [28]. In particular, the piezoelectric effect induced by external forces may effectively separate free carriers (electrons and holes), combine with PEC, and increase PEC efficiency. Previous research has reported materials for environmental purification based on the synergy of piezoelectric and photoelectric effects, such as g-C$_3$N$_4$, BiOBr, BaTiO$_3$, and PbTiO$_3$ [29–31].

As a new type of material with both optoelectronic and piezoelectric effects, sodium bismuth molybdate (NaBi(MoO$_4$)$_2$) has an AB(CO$_4$)$_2$ (A=Na, K, *etc.*, B=Bi, La, *etc.*, C=Mo, W) chemical formula and is a double molybdate or double tungstate inorganic scintillator that combines the advantages of high energy radiation resistance [32], fast optical time response, optical material density and high material luminous efficiency. Novel rare-earth laser photonic-crystal media are frequently used in high-precision optical instruments and equipment [33]. NaBi (MoO$_4$)$_2$ has essential applications in optical safety inspection, optical exploration equipment in the petroleum industry, medical optics, and the development and use of optical devices for high-energy physics. Furthermore, NaBi(MoO$_4$)$_2$ is a n-type semiconductor material with a band gap width of 2.8–3.1 eV, that may be excited by photons with the greatest visible photon energy or the lowest UV photon energy and can therefore be used as photocatalysts for the degradation of organic pollutants [34]. It is also considered to be a piezoelectric crystal owing to its non-centrosymmetric $\overline{I4}$ space group [27]. MoS$_2$ is also a kind of semiconductor material with both photoelectric properties and a piezoelectric effect [35–41]. MoS$_2$ can be classified explicitly into 1T, 2H, and 3 R phases based on its underlying phase state and the stacking order of its layers in the cell [31,42–47]. As a special form of MoS$_2$, MoS$_2$ quantum dots(QDs) have low biotoxicity, outstanding photoelectric and chemical catalytic activity, high photoelectric conversion quantum yield, strong resistance to photobleaching, and excellent as well as stable photofluorescence performance are remarkable and excellent [48]. Sun et al. obtained MoS$_2$ QDs *via* a liquid exfoliation strategy with a rate of 0.206 mmol h^{-1}•g^{-1} and obtained photocatalytic hydrogen production activity photocatalytic, surpassing that of CdS [49]. However, the catalytic efficiency of semiconducting 2H phase MoS$_2$ QDs co-catalysts with low intrinsic conductivity is still constrained. Highly conductive metal 1T-phase MoS$_2$ QDs can facilitate fast injection-transfer and electron-charge injection-transfer in photocatalytic processes, but they lack the properties of semiconductors [48]. The preparation of metallic 1T-phase MoS$_2$ quantum dots (denoted as 1T MoS$_2$ QDs) is a direct approach to solve this fundamental problem because metallic 1T MoS$_2$ QDs with high conductivity can facilitate fast injection-transfer and electron-charge in photocatalytic HER processes. Zhang et al. have investigated 1T MoS$_2$ QDs [50], demonstrating remarkable HER performance in the electrochemical 70% composition 1T phase of 1T MoS$_2$ QDs. Although the 1T MoS$_2$ QDs achieved impressive electrocatalytic performance, the preparation of 1T MoS$_2$ QD with a high ratio was tedious, complicated, and time-consuming. Pioneering work has mostly focused on a single 2H or 1T phase, seldom focusing on composites of 1T

and 2 H MoS$_2$ QDs. Furthermore, MoS$_2$ has been applied as a potential piezoelectric photocatalyst because of its easily deformable layered structure, abundant edge active sites, and narrow band gap (1.65 eV) [51,52]. Wu et al. prepared polymorphic MoS$_2$ nanoflowers with different piezoelectric capacities of 1T, 2H, and 1T/2H MoS$_2$ nanoflowers [53].

Stainless steel mesh(SSM) is an ideal electrochemical engineering current-collector for electrode manufacturing [54] because of its high electrical conductivity, low manufacturing cost, and mechanical flexibility [55,56]. During this process, the SSM hole size, mesh size, and mechanical structure can be adjusted according to specific requirements [57–59]. Since mutual movement between the electrolyte and the electrolyte ions improves their electrochemical properties [60]. The pressed tablet electrode is an extension and improvement of the material-bonded powder electrode, and it is often used to produce half electrodes for the preparation of button batteries [60]. However, little research has been conducted on the combined applications of stainless steel mesh and pressed tablet electrodes.

In this study, the n-type semiconductor NaBi(MoO$_4$)$_2$ (NBMO) with optoelectronic and piezoelectric effects, was used as a substrate electrode material for a pressed tablet stainless-steel mesh(PT-SSM) photoanode. First, doping and composite modifications of NaBi(MoO$_4$)$_2$ were performed, with heavy rare earth Y^{3+} ion doping modifications in the first step, followed by a multi-phase state (1T, 2H and 1T-2H) MoS$_2$ QDs (MSQD) composite modification by multi-interface polarization engineering. Crystallography, morphology, spectroscopy, wave spectroscopy, and electrochemistry were used to characterize all electrode materials, and density functional theory (DFT) calculations were used to analyze them. The mechanical flexibility of the stainless-steel mesh was then utilized to dexterously combine the piezoelectric effect with PEC in a designed 1T-2H MSQD/Y-NBMO PT-SSM photoanode. A photoanode was used to investigate the environmental purification efficacy of PDE-5i PZ-PEC degradation. The mechanism of Sildenafil degradation *via* PZ-PEC was thoroughly investigated using UPLC-MS/MS analysis of the PDE-5i degradation process and computational analysis of the reactive site of PDE-5i using the condensed Fukui function (CFF) based on the frontier molecular orbital (FMO) theory. The ecotoxicity and biodegradation probability of byproducts from the PZ-PEC process were estimated. Finally, we elucidated the mechanism for the gradual improvement of PZ-PEC performance, which was based on the formation of a built-in electric field of a multiple heterostructure with two types of S-scheme heterojunctions and piezoelectric polarization effects. This work describes a novel and skillful approach for combining the piezoelectric effect derived from mechanical force with PEC generated from visible light illumination and direct-current external bias for environmental purification.

2. Experimental method

2.1. Chemical reagents

In this work, all the synthesis and analysis used Chemical Reagents were unpurified analytical degree. Bismuth nitrate pentahydrate (Bi (NO$_3$)$_3$·5 H$_2$O), Ammonium orthomolybdate ((NH$_4$)$_2$MoO$_4$), Sodium molybdate dihydrate (Na$_2$MoO$_4$·2 H$_2$O), Polytetrafluoroethylene emulsion (PTFE emulsion), Sildenafil Citrate (C$_{22}$H$_{30}$N$_6$O$_4$S·C$_6$H$_8$O$_7$), Tadalafil (C$_{22}$H$_{19}$N$_3$O$_4$), Vardenafil hydrochloride (C$_{22}$H$_{32}$N$_6$O$_4$S·HCl) were supplied form Shanghai Macklin Biochemical Technology Corporation Ltd (Shanghai, China). Sodium sulphate (Na$_2$SO$_4$), yttrium nitrate hexahydrate (Y(NO$_3$)$_3$·5 H$_2$O), L-cysteine (C$_3$H$_7$NO$_2$S), and absolute ethyl alcohol (C$_2$H$_6$O), potassium bromide (KBr), propan-2-ol (C$_3$H$_8$O, IPA), Sodium oxalate (Na$_2$C$_2$O$_4$), L-tryptophan (C$_{11}$H$_{12}$N$_2$O$_2$) were supplied form Shanghai Aladdin Biochemical Technology Corporation Ltd (Shanghai, China). 4-hydroxy-2,2,6,6-tetramethyl-piperidinooxy (C$_9$H$_{18}$NO$_2$ *, TEMPOL), 5,5-dimethyl-1-pyrroline nitrogen-oxide (C$_6$H$_{11}$NO, DMPO) were supplied form Sigma-Aldrich Corporation. Ltd

(USA).

2.2. Preparation of photoelectrode material and SSM pressed tablet electrodes

Preparation of NaBi(MoO$_4$)$_2$ (NBMO) and the composite electrode materials: Adding 9.68 g Na$_2$MoO$_4$·2 H$_2$O and 9.70 g Bi(NO$_3$)$_3$·5 H$_2$O in 160 ml deionized water, mixing and stirring for more than a half hour until the color of the mixed solution become a pale green-white suspension. Transfer the mixed solution to a hydrothermal synthesis reactor with 200 ml at 180 °C for 24 h, then pour out the supernatant and centrifuge (10,000 r/min) for 30 min to precipitate the pale green-white solid. Afterwards, the supernatant was poured out and the precipitated white solid was washed by centrifugation (10,000 r/min) and anhydrous ethanol washing 30 with three cycle times. After completion of the above steps, the concrete was removed from to a surface dish and transferred to a drying oven for 12 h at 60 °C. Based on this step mass manufacturing and collecting NBMO samples for analytical testing and next-step modification.

The primary modified-step was similar to the NBMO synthesis, Y (NO$_3$)$_3$·5 H$_2$O was added to the mixed suspension before hydrothermal, with doping ratios were reported in the literature molar ratios (Measurement reference was Na$_2$MoO$_4$·2 H$_2$O) of 0.5%, 1.0%, 1.5%, 2.0% and 2.5%, respectively. Five different doping ratios of rare earth Y^{3+} ion-doping NBMO electrode materials were produced by the same one-step hydrothermal method with the same reaction temperature, time and purification procedure as NBMO synthesis. The samples in the primary modified step were named as 0.5Y-NBMO, 1.0Y-NBMO, 1.5Y-NBMO, 2.0Y-NBMO and 2.5Y-NBMO. After that in the modified secondary step, 1.5Y-NBMO synthesized in the previous step and showed the best photoelectric property (as shown in Fig. S1), was used as the base material. And the MoS$_2$ QDs the synthesis by bottom-up method, dissolving 0.586 g (NH$_4$)$_2$MoO$_4$ in 80 ml of deionized water, ultrasonicated for 5 min, then added 1.6 g L-cysteine (C$_3$H$_7$NO$_2$S), continued to ultrasonicate for 20 min. Afterward, adding 5 g 1.5Y-NBMO and another 80 ml deionized water to the black solution, then tansferred to a hydrothermal synthesis reactors to synthesize composites at different temperatures of 180 °C, 200 °C, and 220 °C by a mass fraction as reported in the literature. The two-step modified electrode material samples were named as 1T MSQD/1.5Y-NBMO, 2H MSQD/1.5Y-NBMO, 1T-2H MSQD/1.5Y-NBMO, which were decided by the dominated ratio of 1T or 2H type MoS$_2$ QDs the electrode materials contained.

Preparation of the pressed tablet stainless steel mesh (PT-SSM) electrode: The 4 cm diameter circular stainless-steel mesh (SSM, 200 mesh, 304 stainless steel grade for corrosion protection) was used as a current-collector. The electrode material from all the samples prepared in the above steps, with PTFE emulsion and acetylene carbon black of electronic grade are mixed in the ratio of 0.05–0.25 g, 200 μL and 0.02 g to make a viscous paste of electrode material precursor. Then the precursors were coated and spread evenly around the middle of the SSM, dried in a plate heater at 80 °C for 10 min, placed on ultra-thin sulfate material on each side of the coated electrode, and placed in the appropriate die to be pressed tablet by tablet machine. All the PT electrodes with great mechanical flexibility are produced by holding the front and back sides at 10 kPa for 30 s. All the samples mentioned above were built up as PT electrodes in this method. The processes were shown in Scheme 1.

2.3. Characterization

For morphology characterization, the field emission scanning electron microscopy (FESEM) characterization and elemental mapping were
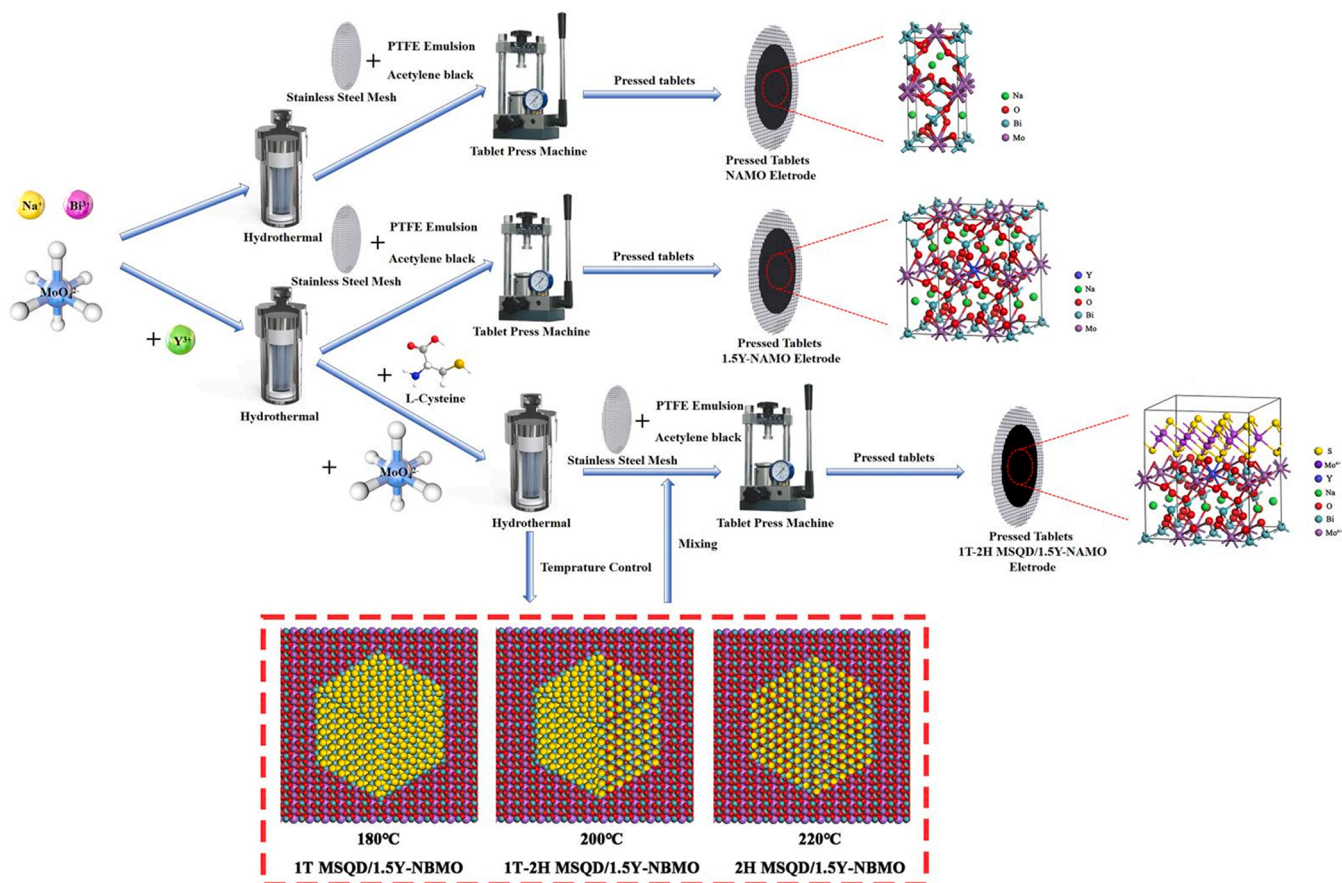
Scheme 1. Schematic diagram for preparation of electrode materials and PT-SSM electrodes.

tested on FEI XL-30 ESEM FEG scanning electron microscope. The field emission transmission electron microscopy (FETEM), SEAD, and EDS characterization were carried out on the FEI Tecnai-G2–20 transmission electron microscope. X-ray powder diffraction (XRD) was tested on an X/max-RA Advance diffractometer using CuKα radiation. FTIR spectroscopy was carried on a Nicolet 550 Fourier transform infrared spectrometer over a wavenumber range of 500–4000 cm^{-1}. Raman spectroscopy was carried on a LabRam HR Evolution; Horiba Scientific; renishaw inVa; Thermo Fischer DXR Raman Spectrometer. X-ray photoelectron spectroscopy (XPS) and XPS valence band spectrum analyzed were tested on a Thermo ESCALAB 250 spectrometer with an AlKα (1486.6 eV) and MgKα (1253.6 eV) mono X-ray source. UV-Vis diffuse reflectance spectroscopy (UV-Vis DRS) was operated on a UV-Vis-NIR spectrophotometer UV3600. Photoluminescence (PL) spectroscopy and Time-resolved photoluminescence (TRPL) were tested on steady-state transient fluorescence spectrometer FLS1000/FS5. Electrochemistry Study of Electrochemical impedance spectroscopy (EIS), Mott-Schottky plots, Tafel curve, Cyclic voltammetric curves, I-V polarization curve and photocurrent density was tested on CHI660E electrochemical workstation and the analyzer. Piezoresponse Force Microscopy (PFM) was carried on MFP-3D Piezoresponse Force Microscopy. Electron spin resonance spectrum was carried on Bruker-A200 Electron Spin Paramagnetic Resonance spectrometer, with 6.33 mW power, 9.75 GHz microwave frequency, 3500 G central field strength of 3500 G, and 150 G scan width.

2.4. Piezoelectric-photoelectrocatalysis properties test

The circumstance of visible light was created by a xenon lamp (PLS-SXE300/300 UV, 300 W, Beijing PerfectLight) with a ultraviolet removed filter lens (wavelength λ < 420 nm). The prepared pressed electrodes were clamped with SSM electrode clips and connected to the positive terminal of a DC Voltage Regulator (SBW DC, Shanghai Voltage Stabilizer Factory) with a red wire as a photoanode, the black wire was connected to the negative terminal of the SBW DC regulated power supply and attached to the same SSM electrode clips as the cathode for the condition of DC External bias. Fig.S2 d showed various physical diagrams of the PZ-PEC system, usually with 1.5 V voltage and 0.05 M Na$_2$SO$_4$ electrolyte as the PZ-PEC test background, and put into a detachable photoelectrochemical cell with 85% light transmission for the PZ-PEC degradation test. The rotational mechanical force of magnetic rotor was applied to support the piezoelectric process by adjustable magnetic stirrer. The PEC performance of electrode samples was estimated *via* the degradation efficiency of contaminant. The main target PDE-5i contaminant for degradation in this work was Sildenafil Citrate (C$_{22}$H$_{30}$N$_6$O$_4$S·C$_6$H$_8$O$_7$), which was prepared with ultrapure water at a concentration of 10 mg/L for PZ-PEC property comparison of Y^{3+} ion-doping NBMO electrode materials and 25 mg/L for PZ-PEC property comparison of MoS$_2$ QDs-modified 1.5Y-NBMO electrode materials. The other two amcinonide contaminants were Tadalafil (C$_{22}$H$_{19}$N$_3$O$_4$) and Vardenafil hydrochloride (C$_{22}$H$_{32}$N$_6$O$_4$S·HCl), which were prepared at 25 mg/L with ultrapure water adjusting the concentrations, respectively. Since the spectral characteristics of PDE-5i in a complex system were not obvious, the concentration and intermediate products of contaminants were detected by the UPLC-MS/MS method carried on AB Sciex UPLC-QTRAP 6500 mass spectrometry detector with Athena C18-WP chromatographic column (The unique details of the test were shown in Text S1) during the PZ-PEC degradation process. For testing the robustness of the photoanode, the used sample-electrodes were washed with an ethanol and ultrapure water under low-intensity ultrasound (50 W), and then dried. Each sample-electrodes were carried out, and standard errors were estimated at least five cycles. The equation for calculating the PEC efficiency (η, %) of Sildenafil was Eq. (S1). The Multi n/c 3100 TOC/TN detector was applied to estimate total organic carbon (TOC) content. The single piezoelectric process and PEC process were carried on the same circumstance.

Furthermore, to investigate the free radical mechanism of the PEC process, we performed EPR radical trapping experiments on the experiments and determined the contribution of reactive species. We used a selection of drugs as our free radical trapping agents by using IPA, Na$_2$C$_2$O$_4$, TEMPOL, L-tryptophan, as quenchers of·OH, h$^+$,·O$_2^-$ and ^{1}O$_2$, and DMPO (10 mM) for free radical trapping, all at a concentration of 10 mM.

2.5. Theoretical computation and ecotoxicity simulation

Density functional theory (DFT) was applied to simulate electronic structures *via* Quantum Espresso version 7.1. For describing the interactions between core and electrons, and the plane-wave expansion of the electronic wave function, the Perdew−Burke−Ernzerhof (PBE) of General Gradient Approximation (GGA) function projector augmented wave (PAW) model combined with the projector augmented wave (PAW) model was employed and an energy cutoff of 450 eV was used. The gamma-point centered Monkhorst−Pack grids were applied to sampling in all Brillouin zone systems. Slab geometry optimizatied by a 2 × 2 × 1 Monkhorst Pack k-point setup. The convergence criteria of force and energy convergence criteria were respectively set up as 0.02 eV/Å and 10^{-5} eV. The specific calculations include energy band structure, the density of state (TDOS and PDOS), differential charge density distribution, and work function.

Simulations of mechanical force effects on piezoelectric response are performed *via* COMSOL multiphysics 6.0. The simulated piezoelectric physical fields belong to the piezoelectric-solid sub-module under the structural mechanics module for electromagnetic-structural interactions, which also contains two sub-modules for solid mechanics and electrostatics, and the Multiphysics properties of these two sub-modules are linked together by Multiphysics field-piezoelectric effects in COMSOL Multiphysics. The physical properties of the material are set up separately in the solid mechanics and electrostatics submodules, which are simulated by Multiphysics field-piezoelectric effects.

For the Fukui function calculation of the Sildenafil molecule, this work used the application of Gaussian 16, revision A.03 and Multiwfn 3.7 to optimize the structure of the sildenafil molecule, the hybrid density flooding theory was used in B3LYP/6–31 G* *. The calculated results used the Multiwfn 3.6 combined with the Visual Molecular Dynamics (VMD) program for wave function analysis, plotting of condensed Fukui function (CFF) isosurface maps and condensed double descriptor (CDD) coloring of molecular surface maps for predicting the reactive sites of contaminants and to characterize fragment molecules. Details of the relevant calculations can be found in text S5.

The EPA Ecoar 2.02 and EPI SUITE-BIOWINNT were applied to predict Ecotoxicity and Biodegrade Probability, which is based on the Quantitative Structure-Activity and Pharmacokinetic Relationship (QSAR and QSPR) model. The relevant Simplified molecular-input line-entry system (SMILES), the corresponding details can be found in the Table S12.

3. Results and discussion

3.1. Morphology and material structure

The SEM and TEM images shown in Fig. 1 depict the morphologies and structures of the different electrode materials. Fig. 1a-c shows SEM images of NBMO, 1.5Y-NBMO, and 1T-2H MSQD/1.5Y-NBMO. All of the electrode materials were stacked with three-dimensional sheets, with an average sheet thickness of approximately, 100 nm, providing ideal conditions for the loading of MoS$_2$ QDs. Fig. 1d-f shows TEM images of NBMO and 1.5Y-NBMO, as well as HRTEM of 1T-2H MSQD/1.5Y-NBMO electrode material. Fig. 1d and e indicate the accumulation of sheet morphology material. Fig. 1f shows the MoS$_2$ QDs loading on the 1.5Y-NBMO electrode material. Fig. 1g,h the lattice distances of 0.310 nm and 0.260 nm are attributed to the (112) and (200) lattice planes of 1.5Y-
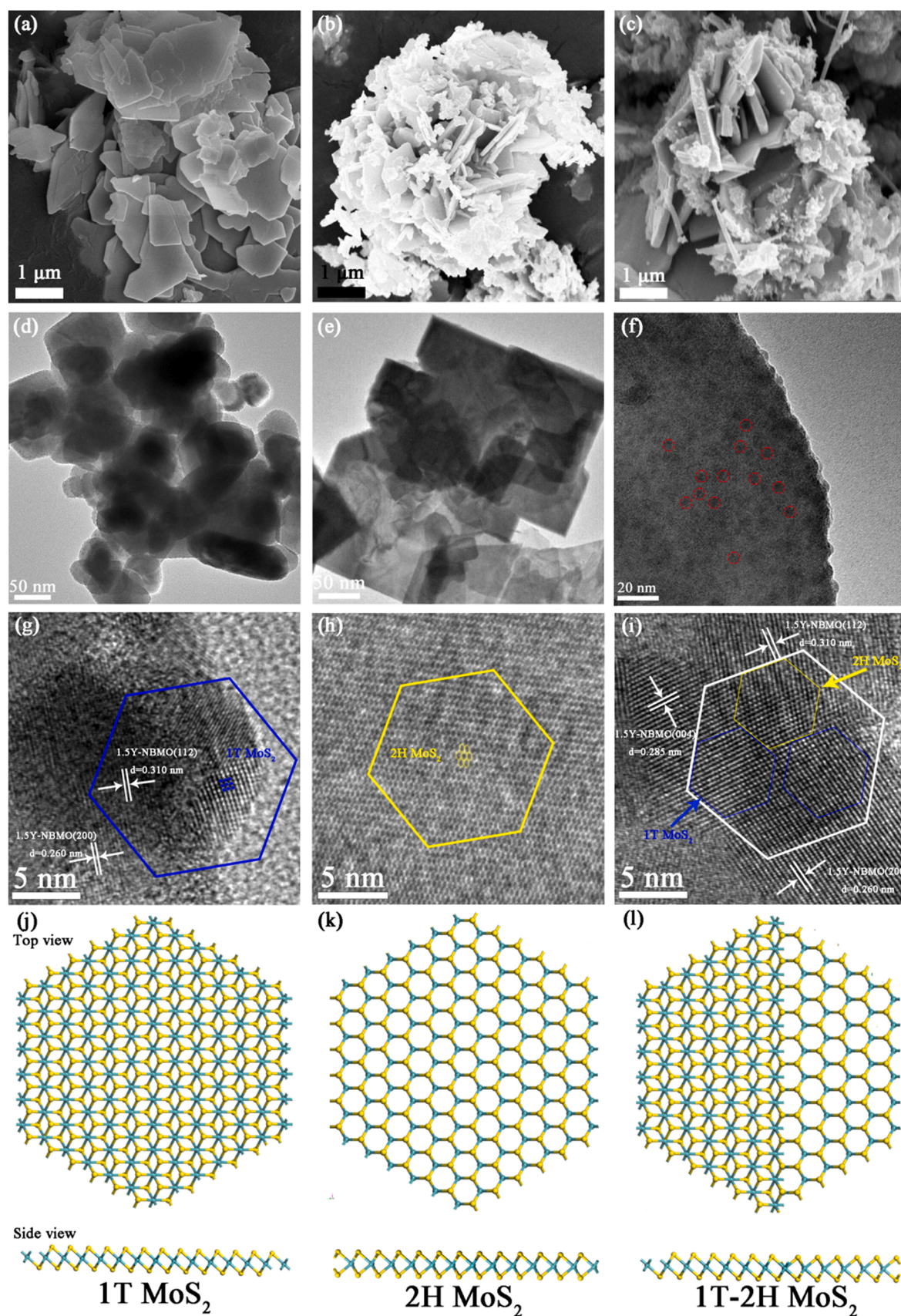
Fig. 1. SEM images of a) NBMO, b) 1.5Y-NBMO, and c) 1T-2H MSQD/1.5Y-NBMO. TEM images of d) NBMO, e) 1.5Y-NBMO, and f) 1T-2H MSQD/1.5Y-NBMO. HRTEM of g) 1T MSQD/1.5Y-NBMO, h) 2H MSQD/1.5Y-NBMO, and i) 1T-2H MSQD/1.5Y-NBMO. Top and side view of crystal structure diagram of j) 1T MoS_2, k) 2H MoS_2, and l) 1T-2H MoS_2.

NBMO, as well as the presence of separate 1T MoS_2 QDs and separate 2H MoS_2 QDs loaded on 1.5Y-NBMO in the inner structure of the 1T-2H MSQD/1.5Y-NBMO, which indicated the formation of 1T MSQD/1.5Y-NBMO and 2H MSQD/1.5Y-NBMO heterostructures. Fig. 1i displays a similar lattice plane of 1.5Y-NBMO, as well as an additional (004) lattice plane with a lattice distance of 0.285 nm. Moreover, both 1T and 2H compound phases of MoS_2 QDs, which we termed 1T-2H MoS_2 QDs in this work, were loaded on the 1.5Y-NBMO, which manifested the formation of 1T-2H MoS_2 and 1T-2H MSQD/1.5Y-NBMO heterostructures. Panels j-l in Fig. 1 correspond to panels g-i, which show the front and lateral views of separate 1T MoS_2 QDs, separate 2H MoS_2 QDs, and 1T-2H MoS_2 QDs, respectively. Fig. 1g-l presents the crystal structures of separate 1T MoS_2 QDs, 2H MoS_2 QDs, and 1T-2H MoS_2 QDs, as well as the configuration of all types of MoS_2 QDs loaded on 1.5Y-NBMO electrode materials. Fig. S3a exhibits the stainless-steel mesh (SSM) current

collector with a diameter of 5 cm, and Fig. S3b shows the PT-SSM electrode with a material cover diameter of 3 cm on the current collector with a diameter of 5 cm. The mechanical flexibility from an arbitrary bending angle is demonstrated in Video 1. Fig. S3b,d shows the dismountable PEC reactor and its overall layout during operation. Video 2 exhibits the overall operation of the device during the PZ-PEC process. Fig. S4a and b show the images of real empty and with materials loading SSM sample electrodes. SEM images of empty SSM sample electrodes are shown in Fig. S4c–e, the spare space of SSM is shown in Fig. S4d with a length and width of 40 and 180 μm, respectively, and Fig. S2e shows 45 μm as the average diameter of SSM. Fig. S4f–h reflect the loading state of materials, which evenly filled in spare space of SSM by the Pressed Tablet method. Fig. S5a,b display the EDS multi-layered elemental mapping image and an electronic image of 1T-2H MSQD/ 1.5Y-NBMO. Fig. S5c–h depicts elemental mapping images of 1T-2H
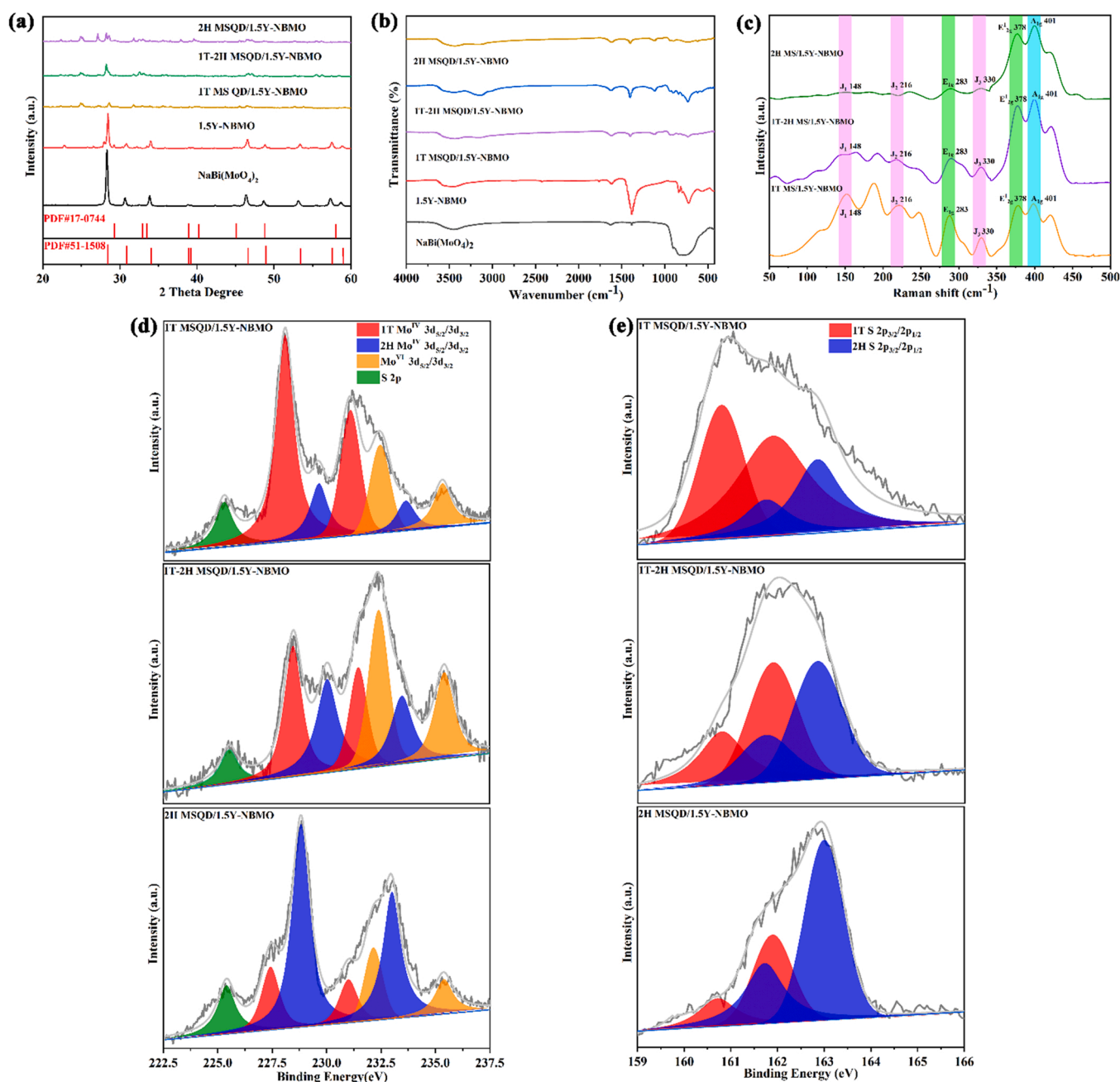

Fig. 2. a) XRD pattern and b) FTIR spectra. c) Raman spectra, d) XPS for Mo and e) S elements of 1T MSQD/1.5Y-NBMO, 2H MSQD/1.5Y-NBMO, and 1T-2H MSQD/ 1.5Y-NBMO.

MSQD/1.5Y-NBMO, which could have even distributions for every element of 1T-2H MSQD/1.5Y-NBMO. The EDX pattern demonstrated that the 1T-2H MSQD/1.5Y-NBMO was free from impurities.

Fig. 2a shows the results of all the electrode material crystal structures by XRD pattern, and the diffraction peaks of 28.39°, 30.80°, 33.94°, 38.88°, 39.30°, 44.92°, 46.48°, 48.75°, 53.36°, 57.51°, and 58.77° are attributed to crystal planes (112), (004), (200), (211), (114) (213), (204), (220), (116), (312), and (224), respectively, which corresponded to the standard card PDF#51–1508 the molybdate series of tetragonal scheelite $NaBi(MoO_4)_2$ in the ICSD crystal database, as well as the monoclinic Y_2O_3 and monoclinic $YO_{1.458}$ diffraction peaks associated with Y^{3+} ion-doping [61–63]. Meanwhile, because of the MoS_2 QDs loading, the diffraction peaks of 29.03°, 32.68°, 33.94°, 33.51°, 35.87°, 39.54°, 44.15°, 49.79°, 55.98°, and 58.33°, were attributed to crystal planes (004), (100), (101), (102), (103), (006), (105), (106), and (110), respectively, clearly corresponding to the hexagonal crystal system standard card PDF#17–0744 crystallographic planes of 2H MoS_2 in the ICSD crystal database in the samples 2H MSQD/1.5Y-NAMO and 1T-2H MSQD/1.5Y-NAMO. Furthermore, Fig. S1a indicates that excessive Y ion-doping can destroy the original crystal properties of NBMO; the main diffraction peaks of 1.5Y-NBMO were masked and reduced, suggesting that the imbalanced loading of 1T and 2H MoS_2 QDs destroyed the original crystalline properties of 1.5Y-NBMO.

Fig. S1b depicts FTIR of the Y^{3+} doped NBMO electrode material samples. The crystalline water -OH stretching vibration peak corresponds to the absorption peak near the wavenumber of 3445 cm^{-1} in the Y^{3+} doped NBMO electrode material sample, the crystalline water H-O-H stretching vibration peak corresponds to the absorption peak at the wavenumber of 1630 cm^{-1} in the Y^{3+} doped NBMO electrode material sample, and the Y-O stretching vibration corresponds to the absorption peak at the wavenumber of 1384 cm^{-1}. The strength and width of the absorption peak increase dramatically as yttrium ion-doping increases, which is attributed to the superposition of the absorption peaks stretching and bending vibrations of the Y-O bonds. The asymmetric stretching and bending vibrations of MoO_6 correspond to the absorption peak around 563 cm^{-1}, whereas the top oxygen atom in the MoO_6 octahedron asymmetric and symmetric stretching vibrations correspond to the absorption peak near 732 cm^{-1}. The stretching and bending vibrations of the Y-O-Y bond correspond to the absorption peak near 564 cm^{-1}, whereas the stretching and bending vibrations of the Y-O bond correspond to the absorption peak near 783 cm^{-1}. According to Fig. 2b, the infrared Fourier spectra (FTIR) results of the MoS_2 QDs/1.5Y-NBMO electrode material samples show absorption peaks near 570 cm^{-1} and 444 cm^{-1} for the stretching vibrations of the Bi-O and Na-O bond, respectively, 563 cm^{-1} for the asymmetric stretching and bending vibrations of MoO_6, and 732 cm^{-1} for the asymmetric and symmetric stretching vibrations of the top oxygen atom of the MoO_6 octahedron. The stretching vibrations of the Y-O-Y bond correspond to absorption peaks near wavenumber 564 cm^{-1}, whereas the stretching vibrations of the Y-O bond correspond to absorption peaks near wavenumber 783 cm^{-1}. Furthermore, the absorption peaks around 956 cm^{-1} and 592 cm^{-1} for the 1.5Y-NBMO materials with disordered MoS_2 QDs were attributed to the stretching vibration of the Mo-S bond, the absorption peaks near 620 cm^{-1} were attributed to the stretching vibration of the Bi-S bond [64], and the absorption peaks around 1120 cm^{-1} and 1290 cm^{-1} were attributed to the asymmetric and symmetric stretching vibration of the S=O bond. The Raman spectrum displays the physical and chemical details of the material compositions. It also revealed that the vibrational patterns E_{1g} (283 cm^{-1}), E_{2g}^1 (378 cm^{-1}), and A_{1g} (404 cm^{-1}) in 1T, 2H, and 1T-2H MoS_2 QDs loading 1.5Y-NBMO were attributed to the characteristics of 2H MoS_2, which are evident in the 2H and 1T-2H MoS_2 QDs loading samples. The vibrational patterns J_1 (145 cm^{-1}), J_2 (210 cm^{-1}), and J_3 (330 cm^{-1}) were attributed to the characteristics of 1T MoS_2, which were clearly present in the 1T and 1T-2H MoS_2 QDs loading samples. The Raman spectrum of 1T-2H MSQD/1.5Y-NBMO demonstrated the coexistence state of 1T and 2H

MoS_2 QDs in the 1.5Y-NBMO electrode material [48,65–76].

Fig. 2d,e shows the XPS patterns of 1T, 2H, and 1T-2H MoS_2 QDs loaded with 1.5Y-NBMO. Gaussian deconvolution fitting peaks at 225.4 eV were attributed to the spin splitting energy orbitals of the S 2p orbital of MoS_2 QDs, fitting peaks at 160.8 eV and 161.9 eV were attributed to 1T $S2p_{1/2}$ and $S2p_{3/2}$, and fitting peaks at 160.8 eV, and 161.9 eV were attributed to 2H $S2p_{1/2}$ and $S2p_{3/2}$ of the 1T, 2H, and 1T-2H MoS_2 QDs loading 1.5Y-NBMO electrode material, respectively. Fitting peaks of the spin splitting energy at 228.4 eV and 231.5 eV were attributed to the Mo(IV) $3d_{3/2}$ orbital and the 1T Mo(IV) $3d_{5/2}$ orbital in 1T, 2H, and 1T-2H MoS_2 QDs loading 1.5Y-NBMO electrode material, respectively. Fitting peaks at 230.0 eV and 233.5 eV were attributed to the spin splitting energy orbitals of the 2H Mo(IV) $3d_{3/2}$ orbital and the 2H Mo(IV) $3d_{5/2}$ orbital in 1T, 2H, and 1T-2H MoS_2 QDs loading 1.5Y-NBMO electrode material. Fitting peaks for the spin splitting energy orbitals at 230.0 eV and 233.5 eV were attributed to the Mo(VI) $3d_{5/2}$ orbital and the Mo(VI) $3d_{3/2}$ orbital of 1.5Y-NBMO electrode material in all sample types [48,77]. Moreover, as shown in Table S1, the fitting peak ratios of 1T Mo(VI), 2H Mo(VI), and Mo(V) were 61.2%, 16.74% and 22.2% in 1T MSQD/1.5Y-NBMO, respectively, with 1T Mo(VI) being dominant. For 1T-2H MSQD/1.5Y-NBMO, the ratios of 1T Mo(VI), 2H Mo(VI) and Mo(V) were 32.9%, 31.36%, and 35.7%, respectively. For 2H MSQD/1.5Y-NBMO, the ratio areas of 1T Mo(VI), 2H Mo(VI) and Mo(V) respectively were 23%, 61.6% and 15.5%, 2H Mo(VI) dominated. Similarly, as shown in Table S2, the fitting peak ratios of 1T MSQD/1.5Y-NBMO, 1T-2H MSQD/1.5Y-NBMO, and 2H MSQD/1.5Y-NBMO were 69.7% (1T S) and 30.2% (2H S), 51.9% (1T S) and 48.1% (2H S), and 32.7% (1T S) and 67.2% (2H S), indicating that the disequilibrium content of 1T MoS_2 QDs or 2H MoS_2 QDs may affect the amount of Mo(VI), thus indirectly affecting the crystal structure of NBMO [78,79]. As shown in Fig. S4 a–f, the fitting peak of the Na1s orbital of Na fitting peak at 1070.60 eV, while the intensity of a considerable decline in this peak in the 1.5Y-NBMO was noted, possibly due to the substitution of the Y ion for the Na lattice site in $NaBi(MoO_4)_2$. The binding energy at 232.28 eV and 235.56 eV fitting peaks was attributed to the $Mo3d_{3/2}$ and $Mo3d_{5/2}$ spin-splitting energy orbits of Mo, and the corresponding fitted peaks at the $Mo3d_{3/2}$ and $Mo3d_{5/2}$ spin-splitting energy levels of Mo in 1.5Y-NBMO were red-shifted by 0.47 eV, indicating that the Y^{3+} modification weakened the interaction between Mo and O [80]. Mo(IV) had binding energies of 228.44 eV and 231.57 eV, S 2p had a binding energy of 225.47 eV, and the fitting peaks $Bi4f_{5/2}$ and $Bi4f_{7/2}$ were 159.10 eV and 164.50 eV, which were attributed to the spin-splitting energy orbits of Bi. the blue shift of Bi4f in 1T-2H MSQD/1.5Y-NBMO attributed the forming of Bi-S bond. The binding energies of the two materials remained constant before and after doping. The fitting peaks at 158.65 eV and 163.96 eV attributed to the $Bi4f_{5/2}$ and $Bi4f_{7/2}$ spin-splitting energy orbitals of Bi. The binding energies of 1 s orbitals of O were at 530.24 eV and 532.36 eV, corresponding to lattice oxygen and oxygen vacancies or OH species, respectively. The doping of Y^{3+} and compounding multi-phase state (1T, 2H and 1T-2H) MoS_2 QDs dramatically increased the proportion of oxygen vacancies, which was favorable for the PZ-PEC reaction.

3.2. OPtoelectric properties

Fig. 3a shows that the NBMO had the maximum PL intensity of the series electrode materials, the 1.5Y-NBMO had the lowest PL intensity, and with the loading of 2H, 1T, and 1T-2H MoS_2 QDs, the PL intensity gradually decreased and reached the minimum in 1T-2H MSQD/1.5Y-NBMO, indicating that the order of the photo-generated hole-electron complex efficiency was 1T-2H MSQD/1.5Y-NBMO, corresponded to the strongest, and NBMO corresponded to the weakest. Furthermore, Fig. S2a,b show the PL spectra and UV-Vis diffuse reflectance spectra of Y^{3+} modified samples, indicating that the 1.5Y-NBMO has the best optical and electronic properties among the Y^{3+} modified samples. The TRPL decay curves of the samples (Fig. 3b) reflect the lifetimes of the
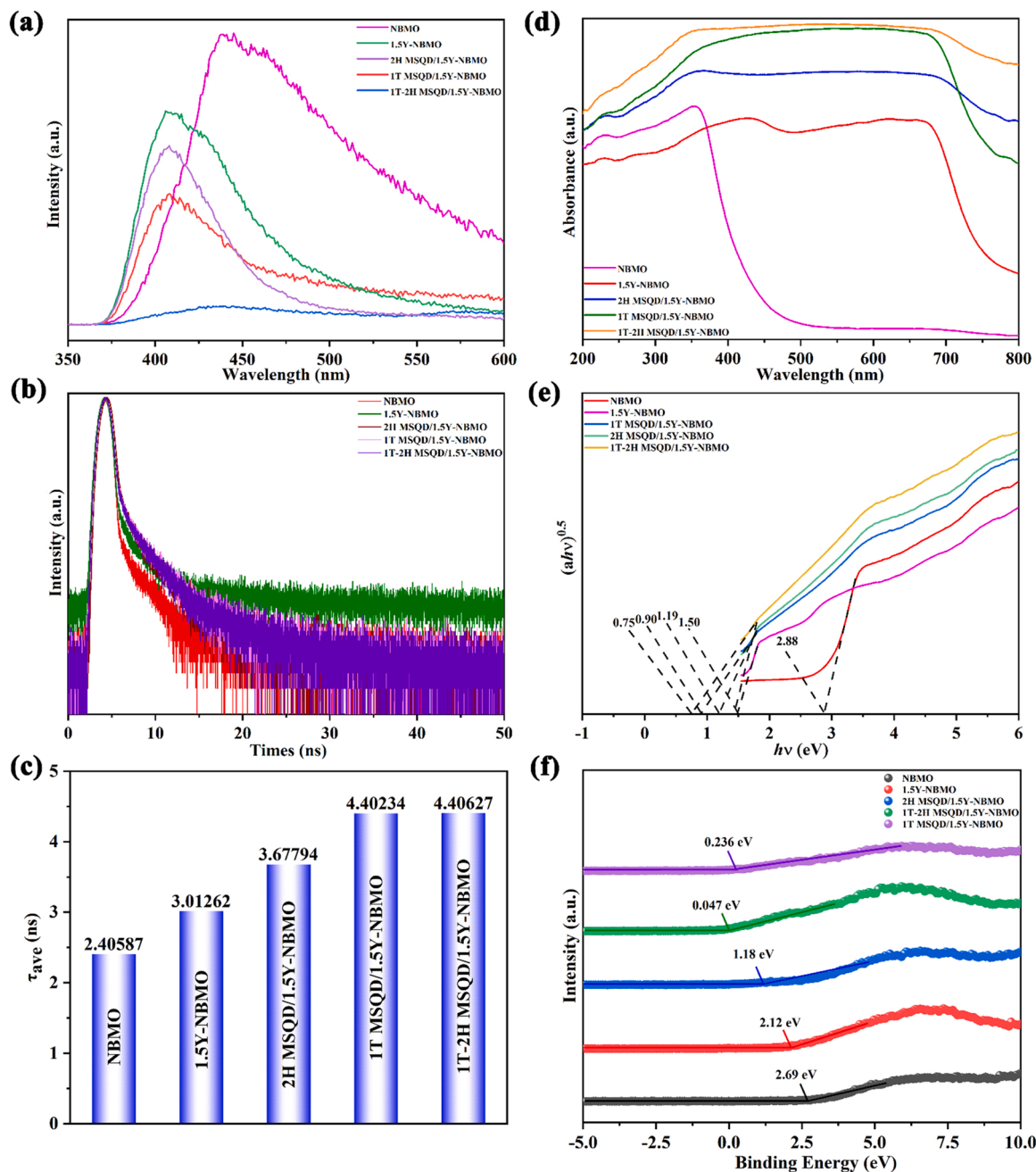
Fig. 3. a) PL spectra, b) TRPL, c) TRPL Timeslife, d) UV-Vis DRS, e) Kubelka-Munk transformed and f) VB-XPS of different samples.

photogenerated electrons of different samples. Fig. 3c shows the calculated average lifetime (τave) of electrons. The τave was datamined for the calculation, shown in Eq. (S3), and was based on the calculated parameters, as shown in Table S3. According to the calculated results, the fluorescence lifetime of 1.5Y-NBMO was 3.02 ns, which was larger than the 2.41 ns of NBMO. The cause of this phenomenon was the doping of Y^{3+}, which inhibits electron and hole recombination. In these corresponding activation reactions, 2H MoS$_2$ increased electron participation and prolonged the electron conduction lifetime of 2H MSQD/1.5Y-NBMO (3.68 ns). The 1T MSQD/1.5Y-NBMO sample exhibited a longer electron fluorescence lifetime (4.40 ns), indicating that 1T MoS$_2$ effectively enhanced the charge carrier separation and transfer. The 1T-2H MSQD/1.5Y-NBMO sample had the longest lifetime (4.41 ns), implying that 1T-2H MoS$_2$ QDs could provide the most robust charge carrier separation and transfer. Fig. 3d shows the solid UV-Vis DRS of the sample materials. As the Fig. S2 b shown, absorption edge red shifts

evidently with the Y^{3+} modification, which reaches the maximum bathochromic-shift of the absorption edge at 700 nm, with the loading of MoS$_2$ QDs, the absorption edge performed more bathochromic-shift, even expand to infrared wavelength, displaying that the 1.5Y-NBMO-based materials have strong absorption in the range from the UV to the visible wavelength. These indicated that both Y^{3+} doping and MoS$_2$ QDs loading help to enhance the absorption of visible light, even at infrared wavelengths. The diffuse reflectance spectra of the 1.5Y-NBMO-based materials were also processed according to the Kubelka−Munk theory (K-M theory) using the Kubelka−Munk metric, as shown in Fig. 3e. The estimated value was based on the tangent of the straight line in the graph extending to the intersection of the horizontal axes. The values of the forbidden bandwidth Eg were 2.88 eV (NBMO), 1.51 eV (1.5Y-NBMO), 1.19 eV (2H MSQD/1.5Y-NBMO), 0.90 eV (1T MSQD/1.5Y-NBMO), and 0.75 eV (1T-2H MSQD/1.5Y-NBMO). This indicates that the appropriate amount of Y^{3+} ion doping is effective not only in

providing the material with certain upconversion properties, but also in compressing the forbidden bandwidth of the material. The valence band spectra of NBMO, 1.5Y-NBMO, 2H MSQD/1.5Y-NBMO, 1T-2H MSQD/1.5Y-NBMO, and 1T MSQD/1.5Y-NBMO were characterized as 2.69 eV, 2.12 eV, 1.18 eV, 0.047 eV, and 0.236 eV by the XPS valence band spectrum following further investigation of the band gap structures of samples.

The I-V polarization curve of NaBi(MoO$_4$)$_2$ based materials is shown in Fig. 4a, with the highest current density reaching 87.9 mA/cm^2 at 1.1 V. According to Fig. 4b, the strengths of the I-V Photocurrent curves were 1T-2H MSQD/1.5Y-NBMO > 1T MSQD/1.5Y-NBMO > 2H MSQD/1.5Y-NBMO > 1.5Y-NBMO > NBMO, suggesting that the strength of the photogenerated photocurrent is minimal for 1T-2H MSQD/1.5Y-NBMO > 1T MSQD/1.5Y-NBMO > 2H MSQD/1.5Y-NBMO > 1.5Y-NBMO > NBMO. Fig. 4c shows the cycling voltametric curves, where the order

of |JRed-1| values is 1T-2H MSQD/1.5Y-NBMO > 1T MSQD/1.5Y-NBMO > 2H MSQD/1.5Y-NBMO > 1.5Y-NBMO > NBMO, and the order of Epp values was NBMO > 1.5Y-NBMO > 2H MSQD/1.5Y-NBMO > 1T MSQD/1.5Y-NBMO > 1T-2H MSQD/1.5Y-NBMO, with 1T-2H MSQD/1.5Y-NBMO electrodes having the best electrocatalytic activity.

The order of the electrochemical impedance arc radii was NBMO > 1.5Y-NBMO > 2H MSQD/1.5Y-NBMO > 1T MSQD/1.5Y-NBMO > 1T-2H MSQD/1.5Y-NBMO, indicating that 1T-2H MSQD/1.5Y-NBMO had the easiest transfer of photogenerated electrons, as shown in Fig. 4d and S7. Fig. 4e shows a Mott-Schottky plot, which estimates the charge carrier density (N$_D$) generated by the slope, as detailed in Eq. (S4). Thus, we represented the charge carrier data by the Mott-Schottky curve of the sample, that is, the density is inversely proportional to the slope. The charge carrier densities of the sample electrodes were classified as follows: 1T-2H MSQD/1.5Y-NBMO > 1T MSQD/1.5Y-NBMO
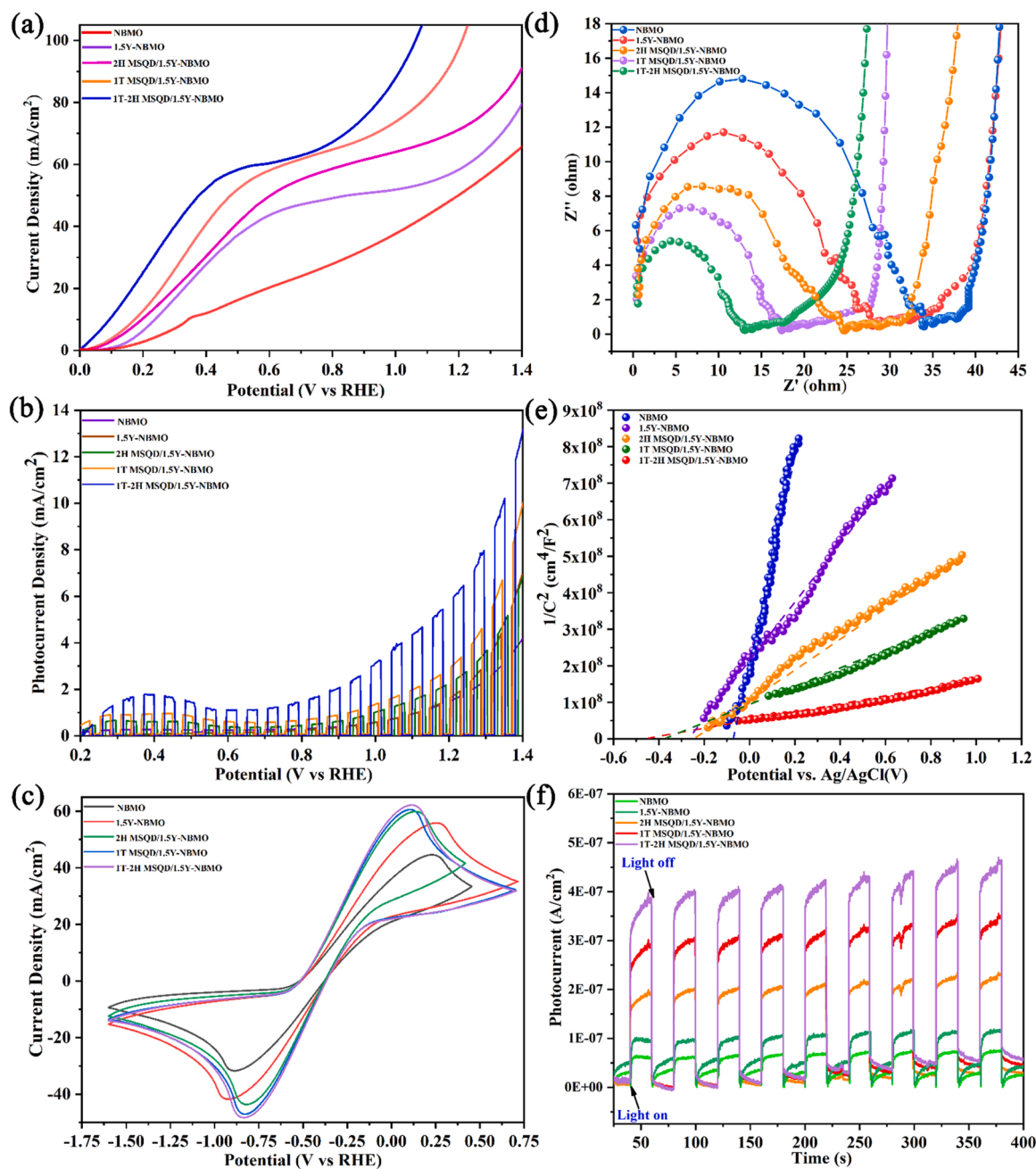

Fig. 4. a) I-V polarization curve b) I-V Photocurrent curve of different PT-SSM photoelectrodes. c) Cyclic voltammetry curve, d) EIS Nyquist curve, e) Mott-Schottky plot, f) I-t Photocurrent curve of different PT-SSM photoelectrodes.

> 2H MSQD/1.5Y-NBMO > 1.5Y-NBMO > NBMO. Fig. 4f displays a comparison of the strength of the I-t curves for 1T-2H MSQD/1.5Y-NBMO > 1T MSQD/1.5Y-NBMO > 2H MSQD/1.5Y-NBMO > 1.5Y-NBMO > NBMO, indicating that the strength of the photogenerated photocurrent was minimal for 1T-2H MSQD/1.5Y-NBMO > 1T MSQD/1.5Y-NBMO > 2H MSQD/1.5Y-NBMO > 1.5Y-NBMO > NBMO. Fig. S7b shows that the Tafel slopes were 146 mV dec^{-1} (NBMO), 97 mV dec^{-1} (1.5Y-NBMO), 69 mV dec^{-1} (2H MSQD/1.5Y-NBMO), 60 mV dec^{-1} (1T MSQD/1.5Y-NBMO), and 41 mV dec^{-1} (1T-2H MSQD/1.5Y-NBMO), reflecting the comparison of charge transfer for different PT-SSM electrodes: 1T-2H MSQD/1.5Y-NBMO > 1T MSQD/1.5Y-NBMO > 2H MSQD/1.5Y-NBMO > 1.5Y-NBMO > NBMO.

3.3. Piezoelectric properties

Piezoresponse force microscopy (PFM) was used to verify the piezoelectric properties of NBMO, 1.5Y-NBMO, 1T MSQD/1.5Y-NBMO, 1T-2H MSQD/1.5Y-NBMO, and 2H MSQD/1.5Y-NBMO photoanode materials. A sharp contrast was observed in their piezoelectric response amplitudes (Fig. 5a1–a3 and S8a1–a2). As shown in Fig. 5b1–b3 and S8b1–b2, the material exhibits piezoelectric-ferroelectric 180° domains within a certain range. As shown in Figs. 5 c1–c3 and S8 c1–c2, the

butterfly loop curve and piezoelectric square hysteresis line with a 180° domain with the voltage is reversed from different voltage ranges (maximun from +60 V to −60 V, and minimum from +15 V to −15 V), implying that 1.5Y-NBMO (93.33 pm/V) had 3.23 times the piezoelectric response amplitude of NBMO (28.89 pm/V). 1T MSQD/1.5Y-NBMO photoanode material exhibited the best piezoelectric ferroelectric properties, with a piezoelectric response amplitude of 340 pm/V, which is 11.77 times that of NBMO (28.89 pm/V), 3.64 times that of 1.5Y-NBMO (93.33 pm/V), 2.13 times that of 1T-2H MSQD/1.5Y-NBMO (160 pm/V), and 3.0 times that of 2H MSQD/1.5Y-NBMO (113.3 pm/V). According to a comparison of the PFM amplitude and voltage results, moderate doping of heavy rare earth Y^{3+} can considerably enhance the piezoelectric properties of NBMO and 1.5Y-NBMO with a multi-phase state (1T, 2H, and 1T-2H) MSQD by interface polarization engineering, and it can cause a differentiated enhancement of the piezoelectric response amplitude for 1.5Y-NBMO.

Fig. 6 shows the COMSOL simulation of the 1T-2H MSQD/1.5Y-NBMO photoanode under different rotational speeds. The maximum stress, surface potential, and multi-sectional electric field values were 4.8×10^5 N/m^2, 30 V and 5.06×10^4 V/m (Fig. 6a1–a3, 360 RPM), 9.5×10^5 N/m^2, 60 V and 1.01×10^5 V/m (Fig. 6b1–b3, 720 RPM), 1.4×10^6 N/m^2, 100 V, and 1.52×10^5 V/m (Fig. 6c1–c3, 1080 RPM).
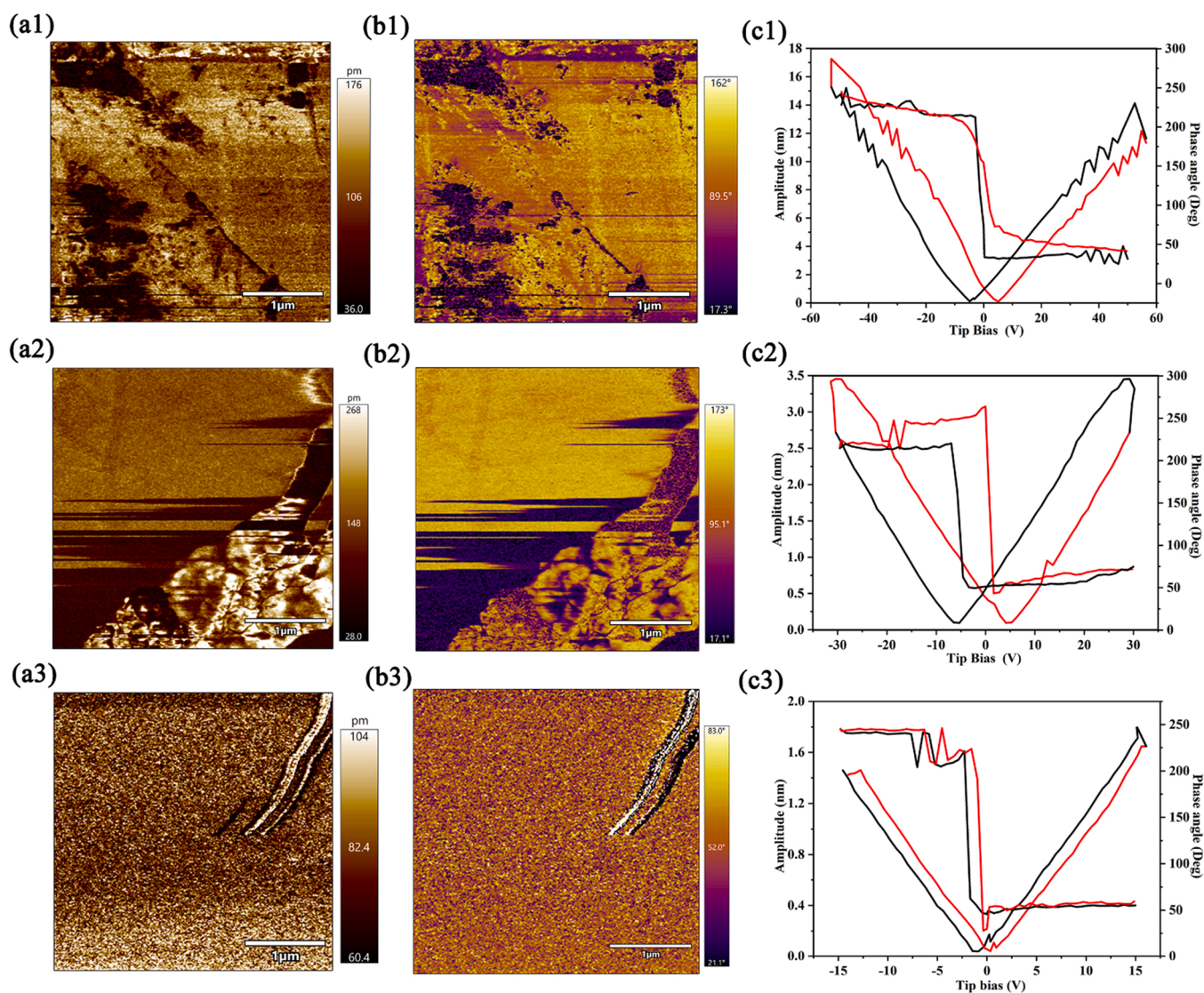

Fig. 5. PFM images of a1-a3) piezoelectric amplitude, b1-b3) phase angle, c1-c3) butterfly loops curve, and piezoelectric hysteresis curve for 1T MSQD/1.5Y-NBMO, 1T-2H MSQD/1.5Y-NBMO and 2H MSQD/1.5Y-NBMO.
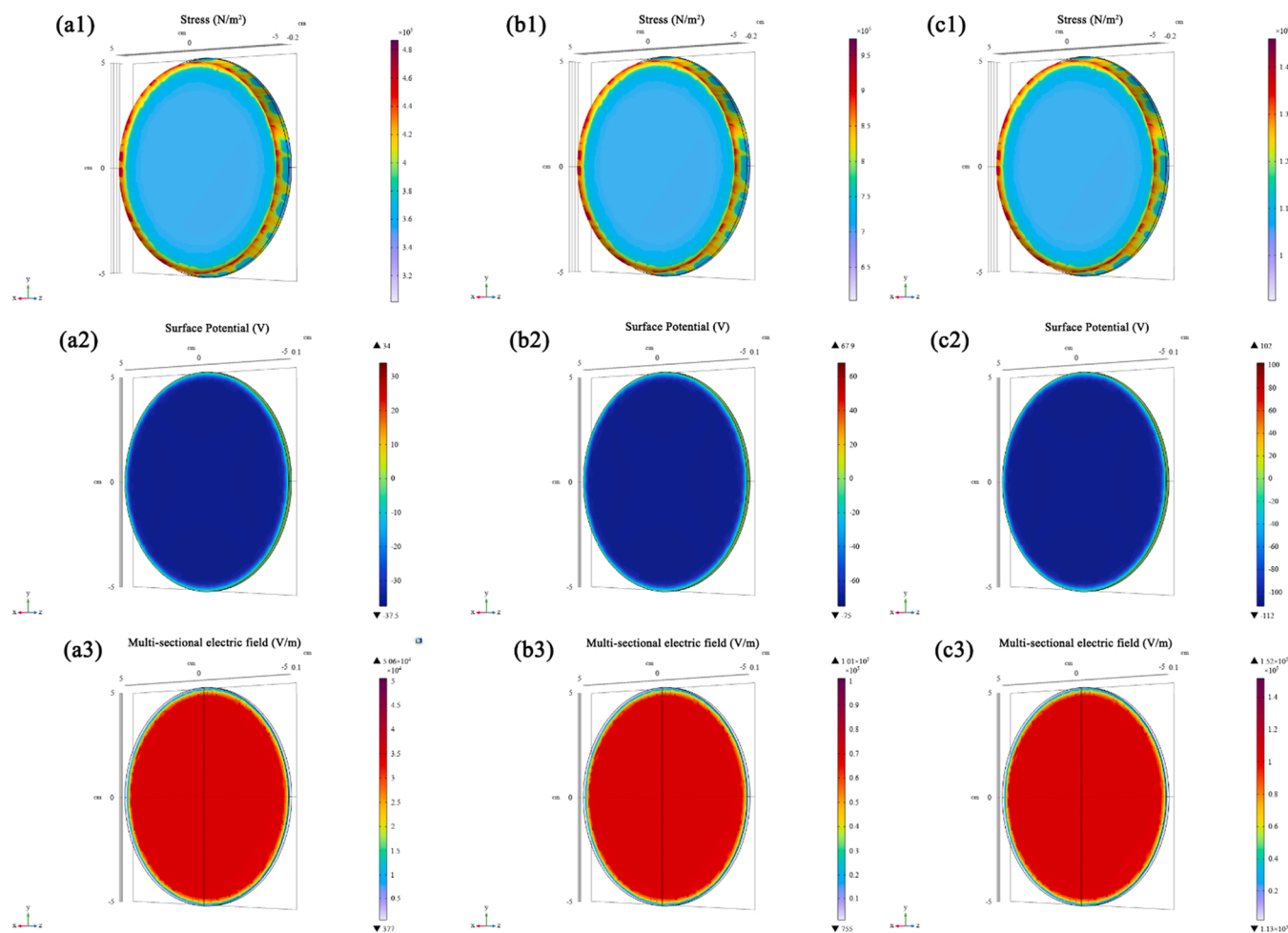
Fig. 6. COMSOL simulation piezoelectric-response of 1T-2H MSQD/1.5Y-NBMO photoanode with conditions of a1-a3) 360 RPM, b1-b3) 720 RPM, c1-c3) 1080 RPM.

Stress, surface potential, and multi-sectional electric field response show similar patterns. The response strength increase with increasing mechanical force, which is consistent with the piezoelectric properties of the material.

3.4. Piezoelectric-photoeletrocatalysis degradation properties and mechanisms

In this study, Sildenafil is used as the main pollutant to evaluate and compare the catalytic degradation properties of different pressed sheet electrodes under different conditions. The single piezoelectric-catalysis and piezoelectric-photoeletrocatalysis processes are shown in Videos 3, 4, and 5. According to Fig. 7a,d, the maximum kinetic constant for single piezoelectric-catalysis are that of the 1T MSQD/1.5Y-NBMO photoanode, which reached $0.01855 \ min^{-1}$ with a degradability rate of 95.5%. As shown in Fig. 7b,e, in the No PEC reaction, Sildenafil exhibited degradability under the conditions of photolysis, photocatalysis, and electrolysis, which were only 5.06%, 19.05%, and 22.56%, respectively, within 50 min under visible light. Under PEC conditions and visible light, NBMO showed the lowest degradation rate of 31.36% with the appropriate doping of Y^{3+}, and the degradation rate of 1.5Y-NBMO electrodes was enhanced to 49.09% within 50 min. After loading the MoS_2 QDs, the degradation rates increased to 76.32% and 84.03% for the 2H MSQD/1.5 Y-NBMO and 1T MSQD/1.5 Y-NBMO electrodes, respectively, within 50 min. Eventually, the 1T-2H MSQD/1.5Y-NBMO electrode achieved a maximum degradation rate of 98.94% within 50 min. Based on Eq. (S5), the 1T-2H MSQD/1.5Y-NBMO PT-SSM electrode clearly exhibits the maximal kinetic constant

($k = 0.0845 \ min^{-1}$), which is almost 13.24 times that of the NBMO electrode. Fig. 7c,f show a maximal kinetic constant ($k = 0.1664 \ min^{-1}$) with a 99.88% degradation rate within 40 min under the piezoelectric-photoelectrocatalytic condition, which is approximately 14.60 times that of the NBMO electrode during the PZ-PEC process. Furthermore, Fig. S3e,f depicts the Sildenafil degradation efficiency of PEC for Y^{3+} modified sample electrodes. The 1.5Y-NBMO electrode had the fastest degradation efficiency and the greatest kinetic constant. Table S4 compares photoeletrocatalysis degradation activity with other photoelectrodes, indicating that the 1T-2H MSQD/1.5Y-NBMO PT-SSM electrode outperformed the others in terms of both kinetics and removal efficiency.

Fig. 7g–i show the response surface of Sildenafil removal efficiency based on external bias voltage, loading amount, and pH. Eq. (S6) is used to represent the final equation in terms of the actual factors for prediction. The response surface of Sildenafil removal efficiency based on external bias voltage, loading amount, and RPM is shown in Fig. 7j–l. When the external bias voltage was 1.0 V, the loading amount was 0.2 g/L, pH was 6.0, and RPM was 1080, we could obtain the maximal Sildenafil removal efficiency of 99.88%. According to Eqs. (S6 and S7), external bias voltage was the strongest factor to influence Sildenafil removal efficiency, followed by loading amount, RPM, and pH. Fig. S10a shows the TOC removal efficiency for PEC and PZ-PEC degradation processes are compared with Sildenafil removal efficiency. The Sildenafil removal efficiency (98.94%) was found to be superior to the TOC removal efficiency (58.65%) for the PEC process, and 99.88% Sildenafil removal efficient vs 12.34% TOC removal efficiency within 50 min. Eventually, the TOC 29.7% removal with PEC process, while the TOC
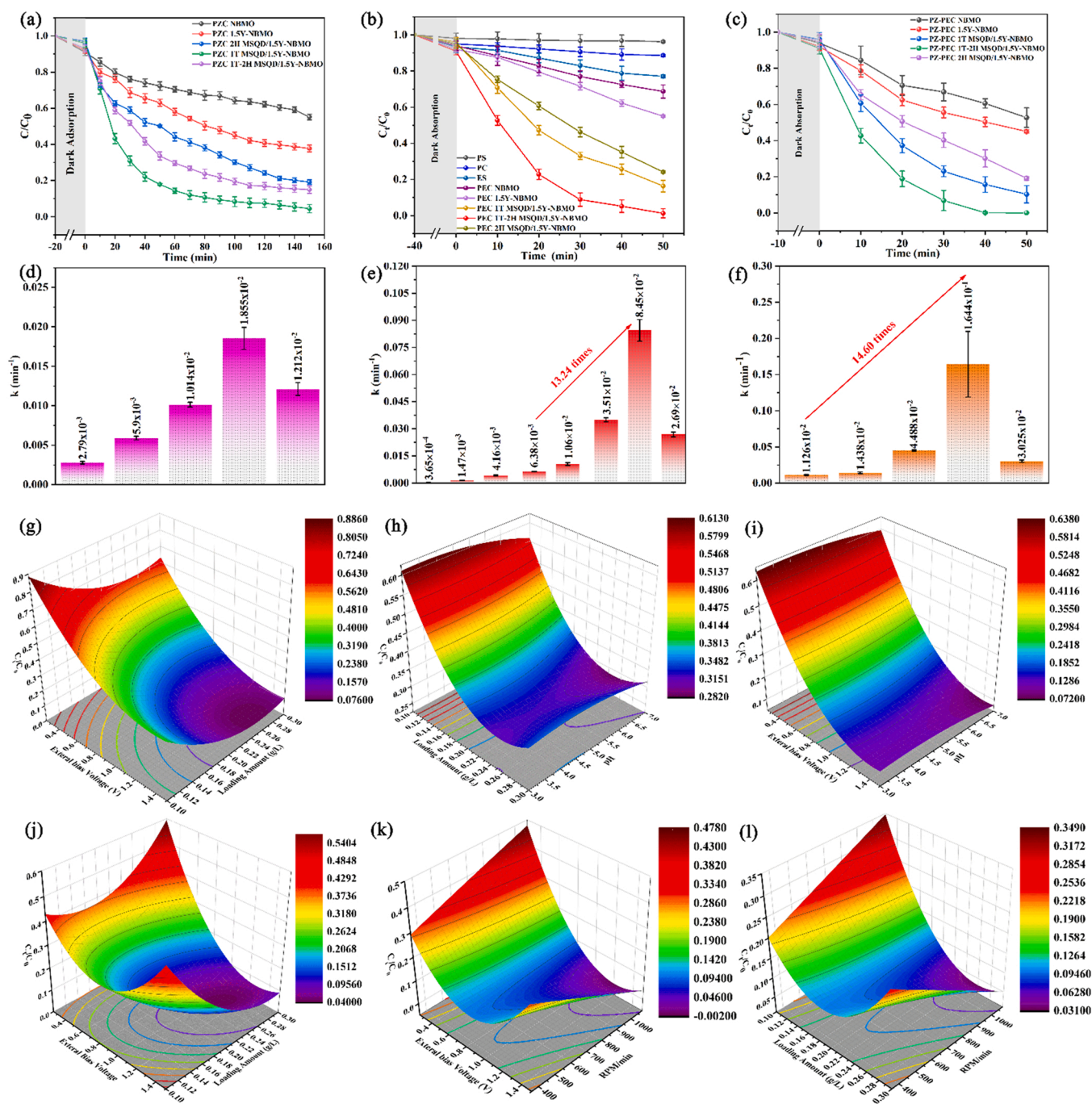
Fig. 7. a) Sildenafil degradation efficiency *via* piezoeletriccatalysis for 1T-2H MSQD/1.5Y-NBMO PT-SSM photoanode. B) Sildenafil degradation efficiency *via* photoeletrocatalysis for 1T-2H MSQD/1.5Y-NBMO PT-SSM photoanode. c) Sildenafil degradation efficiency *via* piezoeletric-photoeletrocatalysis for 1T-2H MSQD/1.5Y-NBMO PT-SSM photoanode. Kinetic constant of d) piezoeletriccatalysis, e) photoeletrocatalysis, and f) piezoeletric-photoeletrocatalysis. Response surface of Sildenafil removal efficiency for g) external bias voltage and loading amount, h) loading amount and pH, and i) external bias voltage and pH. Response surface of Sildenafil removal efficiency for j) external bias voltage and loading amount, k) external bias voltage and RPM, and l) loading amount and RPM.

removal close to 100% with PZ-PEC process within 120 min [81,82]. Fig. S10b compares the degradation curves of Sildenafil, Tadalafil and Vardenafil, with Tadalafil degrading faster than Vardenafil and Sildenafil, which is mainly due to differences in molecular structures. The 1T-2H MSQD/1.5Y-NBMO PT-SSM electrode manifoldly cycles for 30 times, which still maintained 52.8% removal rate after 30 times PZ-PEC cycle degradation, are shown in Fig. S10c. The pH-Zeta potentials of the sample electrodes, as shown in Fig. S10d, were 3.56, 4.91, 5.08, 6.08, and 6.54. Fig. S10e shows long-term PZ-PEC degradation experiments on 1T-2H MSQD/1.5Y-NBMO PT-SSM electrodes under multiple high

concentration conditions, indicating a 100% degradation rate within 50 min for 25 mg/L, 100 min for 50 mg/L, 180 min for 100 mg/L, 13 h for 500 mg/L, and 29 h for 1000 mg/L. As shown in Table S4, the 1T-2H MSQD/1.5Y-NBMO PT-SSM electrode showed superior efficiency in pollutant degradation.

To better understand the radical species involved in the reactions at the 1T-2H MSQD/1.5Y-NBMO electrode. As shown in Fig. 8a, the addition of Na$_2$C$_2$O$_4$, TEMPOL, L-tryptophan, and IPA did not change the PZ-PEC degradation curve of the 1T-2H MSQD/1.5Y-NBMO electrode. Due to the addition of Na$_2$C$_2$O$_4$ to quench holes (h+), the final
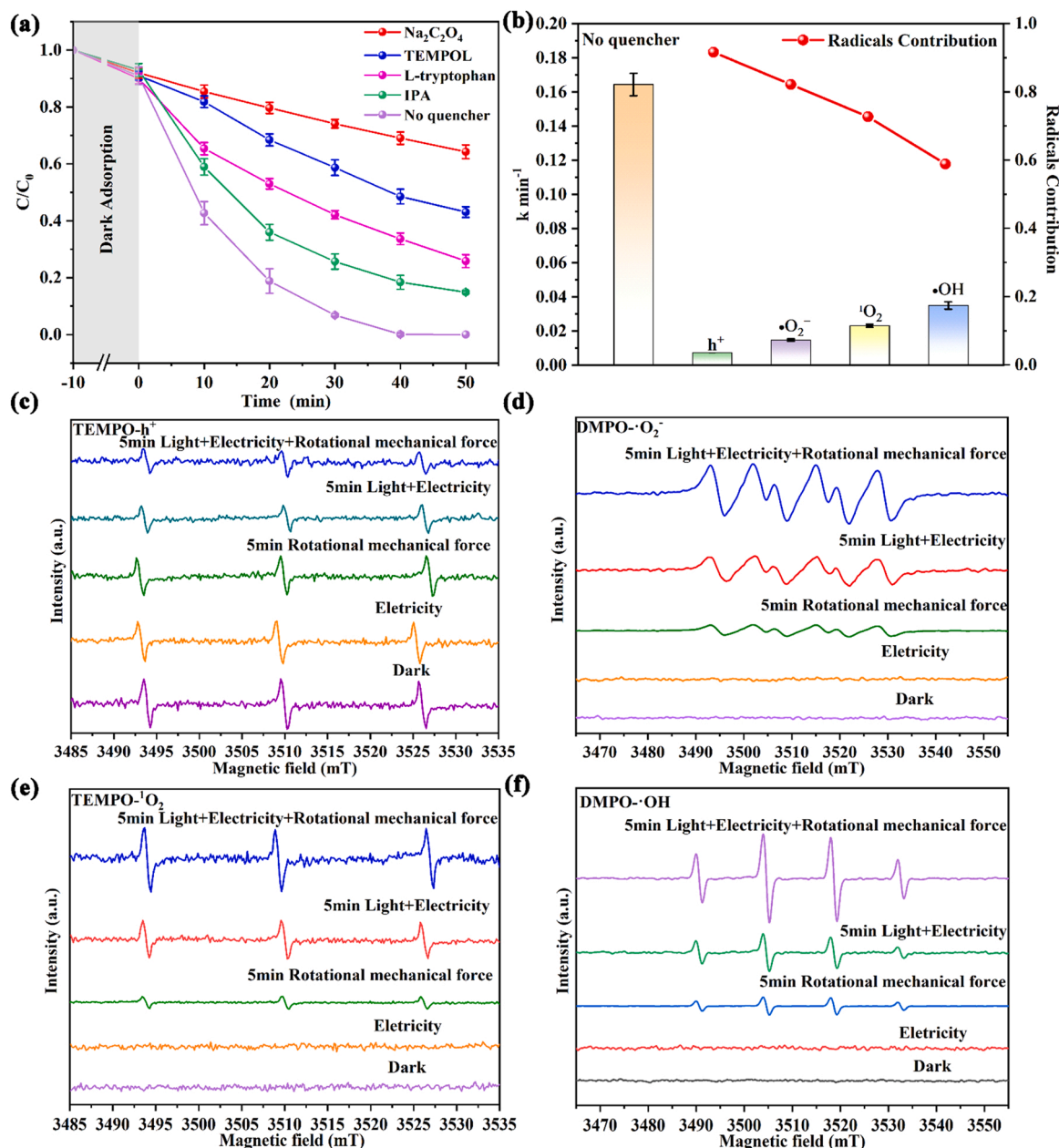
Fig. 8. a) PEC degradation curve of Sildenafil under 1T-2H MSQD/1.5Y-NBMO PT-SSM electrode visible-light irradiation and different quencher conditions. b) Comparison of kinetic constant corresponding to contributions under different quenchers conditions. c) TEMPO-h$^+$ inducers, d) DMPO-•O$_2^-$ inducers, e) TEMP-^{1}O$_2$ inducers, and f) DMPO-•OH adducts for 1T-2H MSQD/1.5Y-NBMO PT-SSM electrode under visible-light irradiation and electricity.

degradation efficiency of Sildenafil within 50 min was only 39.01%, exhibiting a maximal decrease. The addition of TEMPOL and L-tryptophan to quench hydroxyl radicals (·OH), singlet oxygen (^{1}O$_2$), and superoxide radicals (·O$_2$) decreased the degradation by 57.24%, 73.67%, and at least 84.94%, respectively, within 50 min. In the presence of Na$_2$C$_2$O$_4$, the degradation rate constants of TEMPOL, L-tryptophan, and IPA varied considerably at 7.13×10^{-3}, 1.51×10^{-2}, 2.31×10^{-2}, and 3.48×10^{-2} min^{-1}, respectively. Eqs. S6–S9 were used to estimate the rate of contribution of the different data for each radical species. The corresponding rates of contribution of h$^+$, ·O$_2$, ^{1}O$_2$ and ·OH for Sildenafil degradation were 91.56%, 82.13%, 72.66%, and 58.82%, respectively (Fig. 8b). The overall contribution rate exceeded 100%, because of the radical physicochemical reactions involved in PZ-PEC processes. Transformative connections exist between various radical species under various conditions. Therefore, quenching specific free radical species, the radical trap agent, also influenced subsequent transformative

processes, resulting in a contribution exceeding 100%. In general, the most significant radical species generated by the 1T-2H MSQD/1.5Y-NBMO electrode during Sildenafil degradation *via* PZ-PEC was h$^+$, followed by·O$_2$, ^{1}O$_2$, and·OH. DMPO, TEMPO, and TEMP ESR technologies were applied to detect the generation of radical species in the PZ-PEC process. As shown in Fig. 8c, the TEMPO produced a 1:1:1 peak intensity signal. The peak intensity was highest in the dark; with the condition of rotational mechanical force and electricity or light for 5 min only, the peak intensity became slightly weaker; with the time combination of rotational mechanical force, light, and electricity prolonged, the peak intensity decreased, indicating the production of photogenerated h$^+$ in the PZ-PEC process. Similarly, the 1:2:2:1, 1:1:1:1, and 1:1:1 signal peak intensities shown in Fig. 8e–f are attributed to DMPO-·O$_2$, TEMP-^{1}O$_2$, and DMPO-·OH, respectively. Under darkness or electricity, and did not produce any of these three free radical signals. With only light excitation, all of these signal peak intensities emerged

and the signal peak intensity steadily increased under a combination of light, electricity, and rotational mechanical force [82–85].

To better estimate the result of the PZ-PEC process of the 1T-2H MSQD/1.5Y-NBMO PS-SSM electrodes, the process of Sildenafil degradation *via* PEC was analyzed using UPLC-MS. As shown in Fig. 9a, demethylation, de-ethylation, deamination, nitrification, and hydroxylation of Sildenafil molecules readily occurred in the PEC oxidation reaction. 1T-2H MSQD/1.5Y-NBMO PS-SSM electrodes generated large
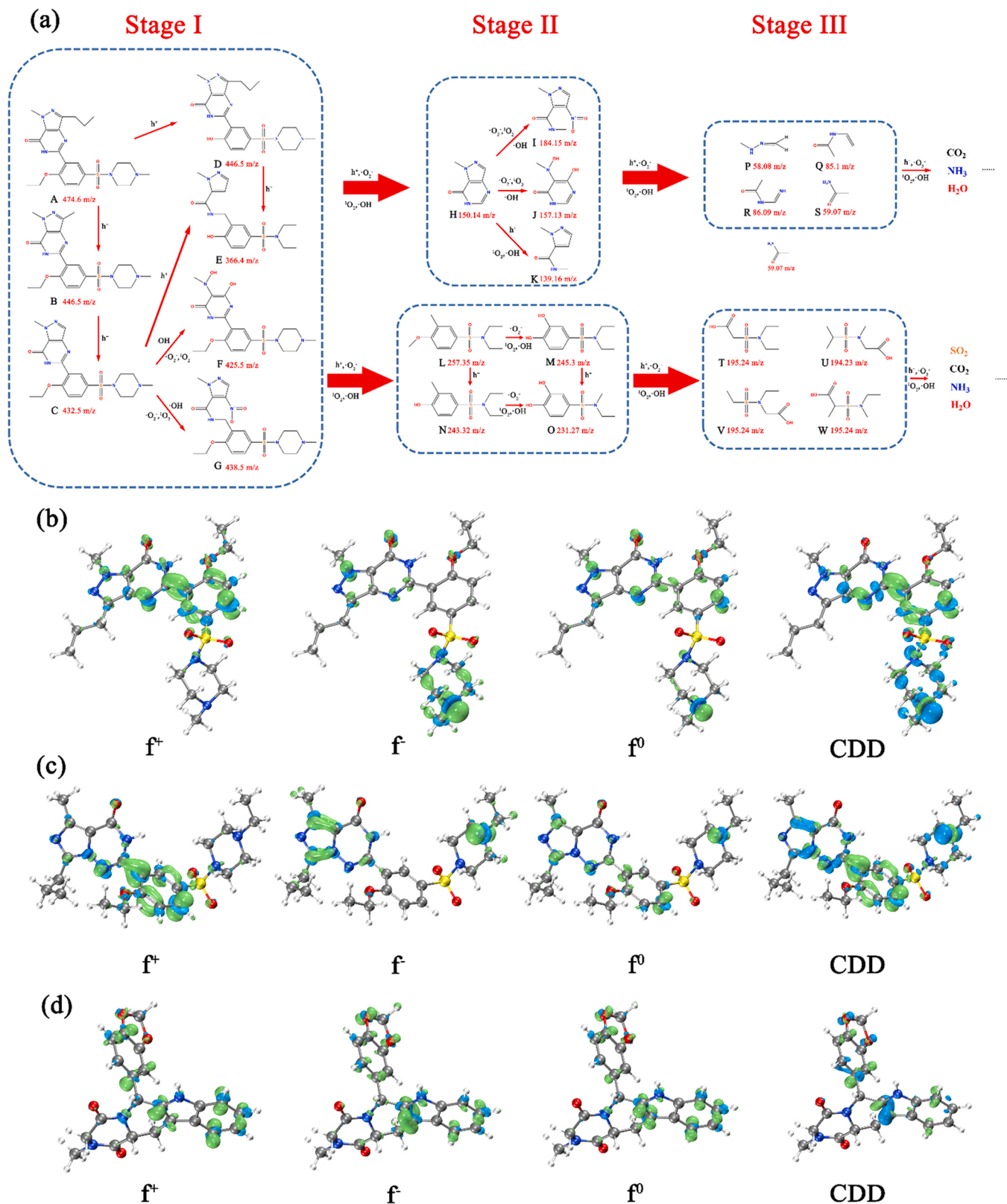
Fig. 9. a) Possible Sildenafil PZ-PEC degradation pathway *via* the 1T-2H MSQD/1.5Y-NBMO PT-SSM electrode. Isosurface of Fukui Index for f$^+$, f$^-$, f^0 and CDD of b) Sildenafil, c) Vardenafil, and d) Tadalafil.

amounts of h^+, $\cdot O_2^-$, $^1O_2$, and $\cdot OH$ to attack Sildenafil molecules during the PEC process (external bias voltage = 1.0 V, loading amount = 0.2 g/L, pH = 6.0, and RPM = 1080). According the UPLC-MS/MS results given in Fig. S11 and Table S12, in Stage I, on the primary pathway, Sildenafil molecule A ($m/z = 474.6$) is attacked by h^+ to form de-ethylation product B ($m/z = 446.5$), and intermediate B is attacked by h^+ to produce demethylation compound C ($m/z = 432.5$). In the secondary pathway, Sildenafil molecule A ($m/z = 474.6$) is attacked by h^+ to form hydroxylation intermediate D ($m/z = 432.5$). Subsequently, intermediate E ($m/z = 366.4$) and intermediate F ($m/z = 425.5$) are synthesized by deamination *via* an h^+ attack and ring-opening reactions with $\cdot O_2^-$, $^1O_2$, and $\cdot OH$ attacks. Intermediate G ($m/z = 438.5$) is produced *via* hydroxylation and nitrification reactions with $\cdot O_2^-$, $^1O_2$ and, $\cdot OH$ attacks, which all come from intermediate C ($m/z = 432.5$). In Stage II, compounds in Stage I are directly or indirectly oxidized into two major types of intermediates, H ($m/z = 150.14$), I ($m/z = 184.15$), J ($m/z = 157.13$), K ($m/z = 139.16$), L ($m/z = 257.33$), M ($m/z = 245.3$), N ($m/z = 243.32$), and O ($m/z = 231.27$), under the attack of h^+, $\cdot O_2^-$, $^1O_2$ and $\cdot OH$ with C-C bond breakage, nitrification, hydroxylation, deamination, and ring-opening reactions. Intermediates I and J are formed by nitrification, hydroxylation, deamination, and ring-opening reactions from product H under $\cdot O_2^-$, $^1O_2$, and $\cdot OH$ attacks, whereas intermediate K is formed by deacylamine reactions under h^+, $^1O_2$ and $\cdot OH$ attacks. Similarly, products M and N are generated by demethylation and hydroxylation reactions of product L, respectively, under the attack of h^+ and $\cdot O_2^-$, $^1O_2$, and $\cdot OH$. Product O is then generated *via* demethylation reactions with h^+ attacks from product M or the demethylation and hydroxylation of $\cdot O_2^-$, $^1O_2$, and $\cdot OH$ attacks from product N. In Stage III, intermediates P ($m/z = 58.08$), Q ($m/z = 85.1$), R ($m/z = 86.09$), and S ($m/z = 59.07$) are principally oxidized by demethylation, de-ethylation, deamination, deamidation, and hydroxylation from products H, I, J, and K, respectively. Intermediates T ($m/z = 195.24$), U ($m/z = 194.23$), V ($m/z = 195.24$), and W ($m/z = 195.24$) were primarily oxidized *via* demethylation, de-ethylation, deamination and hydroxylation from intermediates L, M, N, and O under h^+, $\cdot O_2^-$, $^1O_2$, $\cdot OH$ attacks. All intermediates were eventually mineralized to form the micromolecular gas products SO_2, CO_2, NO_2, NH_3, and H_2O.

To further elucidate the PZ-PEC degradation of Sildenafil, condensed Fukui functions (CFF) based on DFT were used to detect the different reaction types of Sildenafil molecules. The CFF indices f^+, f^-, f^0, and condensed dual descriptors (CDD) correspond to nucleophilic reaction, electrophilic, radical, and nucleophilic electrophilic reactions, respectively. Fig. 9b shows the Fukui index electron density isosurfaces of f^+, f^-, f^0, and CDD. According to Fig. S6 and Table S5, C18 (0.0913), C15 (0.0571), C10 (0.0532), and N9 (0.0563) show relatively high CFF index values in the f^+ CFF index, corresponding to relatively high CFF index values (CDD, C18 (0.0722), C15 (0.0503), C10 (0.0319), and N9 (0.0317)) which were attributed to nucleophilic reactive sites. In the f^- CFF index, O14 (0.0445), N6 (0.0344), C4 (0.0295), and C8 (0.0265) had relatively high CFF index values, but relatively low corresponding CFF index values of CDD, O14 (-0.0017), N6 (-0.0117), C4 (-0.0072), and C8 (-0.0178), which were attributed to nucleophilic reactive sites. For the f^0 CFF index, C18 (0.0552), C15 (0.0503), C10 (0.0372), N30 (0.0559), and N9 (0.0405) were influenced by radical reactive sites. The CFF indicated that nucleophilic, electrophilic, radical, and nucleophilic electrophilic reactive sites were highly correlated with UPLC-MS results. Figs. S12–S14 show the atomic labels of PDE-5i (Sildenafil, Vardenafil, and Tadalafil), and the corresponding isosurfaces for the HOMO and LOMO of PDE-5i are shown in Figs. S15–S17. The isosurfaces for the Fukui indices of Vardenafil and Tadalafil are presented in Fig. 9b–d. The calculated data are displayed in Tables S5, S7, and S9, where Sildenafil performed the minimum among the CFF calculation results for f^+, f^-, f^0, HOMO, LUMO, and molecular hardness, maximum in global molecular softness, but minimum in localized softness s-, which was calculated by Eqs. S12–S14 and shown in Tables S6, S8, S10, and S11, predicted that sildenafil would be difficult to induce the electrophilicity reaction and

be difficult to degrade compared with the other two kinds of pollutants in PDE-5i *via* the PZ-PEC process [86], also reflecting that free radical reactions initiated by the PZ-PEC process are attributed to localized reactions.

The QSAR model was applied to estimate the toxicity and iodegradability of degradation byproducts. As shown in Fig. 10a–c and Table S12, it is evident that the acute toxicity LC_{50} and chronic toxicity ChV for the stage I byproduct are one or two orders of magnitude higher than the original sildenafil molecule. In stage II, the acute toxicity LC_{50} for parts of the byproducts was almost lower than that for the byproducts of stage I. In stage III, the acute toxicity LC_{50} of most byproducts increased, the minority byproducts decreased, and all byproducts became less harmful. The acute toxicity LC_{50} for fish, daphnids, and green algae showed a similar evolutionary trend in the PZ-PEC degradation process, but an order of magnitude lower overall for green algae compared with fish and daphnids, demonstrating an effective reduction of ecotoxicity of Sildenafil by the PZ-PEC process.

As shown in Fig. 11a–c and Table S12, the results of the MITI nonlinear biodegradation and ultimate biodegradation models showed a stepwise evolutionary trend, the biodegradation probability sharply increased from stage I to II, and improved marginally from stage I to II. The results of the nonlinear biodegradation model showed a mountain-like evolutionary trend; the biodegradation probability also sharply increased from stage I to II, but decreased slightly from stage II to III. The PZ-PEC process reduced the concentration and toxicity, and it enhanced the probability of biodegradation of Sildenafil.

To investigate the mechanism of electron transfer between different electron materials, DFT calculations were performed to determine the band gap structure and charge transfer mechanism. Figs. 12a1–a3 and S21a show the DFT calculation model for the NBMO, 1.5Y-NBMO, and 1T-2H MSQD/1.5Y-NBMO electrode materials. According to the DFT calculation of the energy band structure and density of states (DOS), as shown in Figs. 12b1–b3 and S21b–c, the calculated band gap values of NBMO, 1.5Y-NBMO, and 1T-2H MSQD/1.5Y-NBMO electrode materials were 2.881 eV, 1.32 eV, and 0.055 eV, respectively, whereas the experimental test values were 2.94 eV, 1.51 eV, and 0.32 eV, respectively. The calculated findings are slightly smaller than the experimental test findings because the GGA-PBE method for calculating modules underestimates the bandgap values of the calculated semiconductors. Fig. S18a,b shows the energy band structure and DOS of 1T MSQD/1.5Y-NBMO and 2H MSQD/1.5Y-NBMO, which had band gap values 0.12 eV and 0.15 eV. However, the calculated band gap of 1T-2H MSQD/1.5Y-NBMO (0.055 eV) was difficult to obtain by using the GGA-PBE method, which could be due to the restrictions of the DFT method [87–89]. The band gap structures of NBMO, 1.5Y-NBMO, and 1T-2H MSQD/1.5Y-NBMO electrode materials gradually became compressed and more intensive, indicating a considerable enhancement in the number of active electrons, which could have been effectively excited by photons in the ultraviolet, visible, and infrared wavelengths. As shown in Fig. S19a–c, the theoretical DFT calculations for the total density of electron states (TDOS) and partial wave density of states (PDOS), which show that the contributions of each element to the upper conduction bands of NBMO, 1.5Y-NBMO, and 1T-2H MSQD/1.5Y-NBMO electrode materials in the energy range of the band gap were ranked as Mo>O>Bi>Na, Mo>Y>O>Bi>Na, and Mo>Y>O>Bi>S>Na. The contributions of each element to the lower valence bands of NBMO, 1.5Y-NBMO, and 1T-2H MSQD/1.5Y-NBMO electrode materials were in the following order: O>Mo>Bi>Na, O>Mo>Y>Bi>Na, and O>Mo>Y>Bi>S>Na. The contribution of the electronic tracks of each element to the upper and lower conduction bands of the three electrode materials were ranked as $Mo_{4d}>Mo_{4p}>Mo_{4s}>Mo_{3d}$, $Y_{4d}>Y_{4p}>Y_{4s}>Y_{3d}$, $O_{2p}>O_{2d}>O_{1s}$, and $Bi_{6p}>Bi_{6s}>Bi_{5d}>Bi_{4f}$, $S_{3p}>S_{3s}>S_{1s}$, $Na_{3s}>Na_{2p}>Na_{2s}$.

The 1T-2H MSQD/1.5Y-NBMO composite electrode material was investigated using work function calculations for the intrinsic electric field orientation and charge transfer internal driving force. As shown in
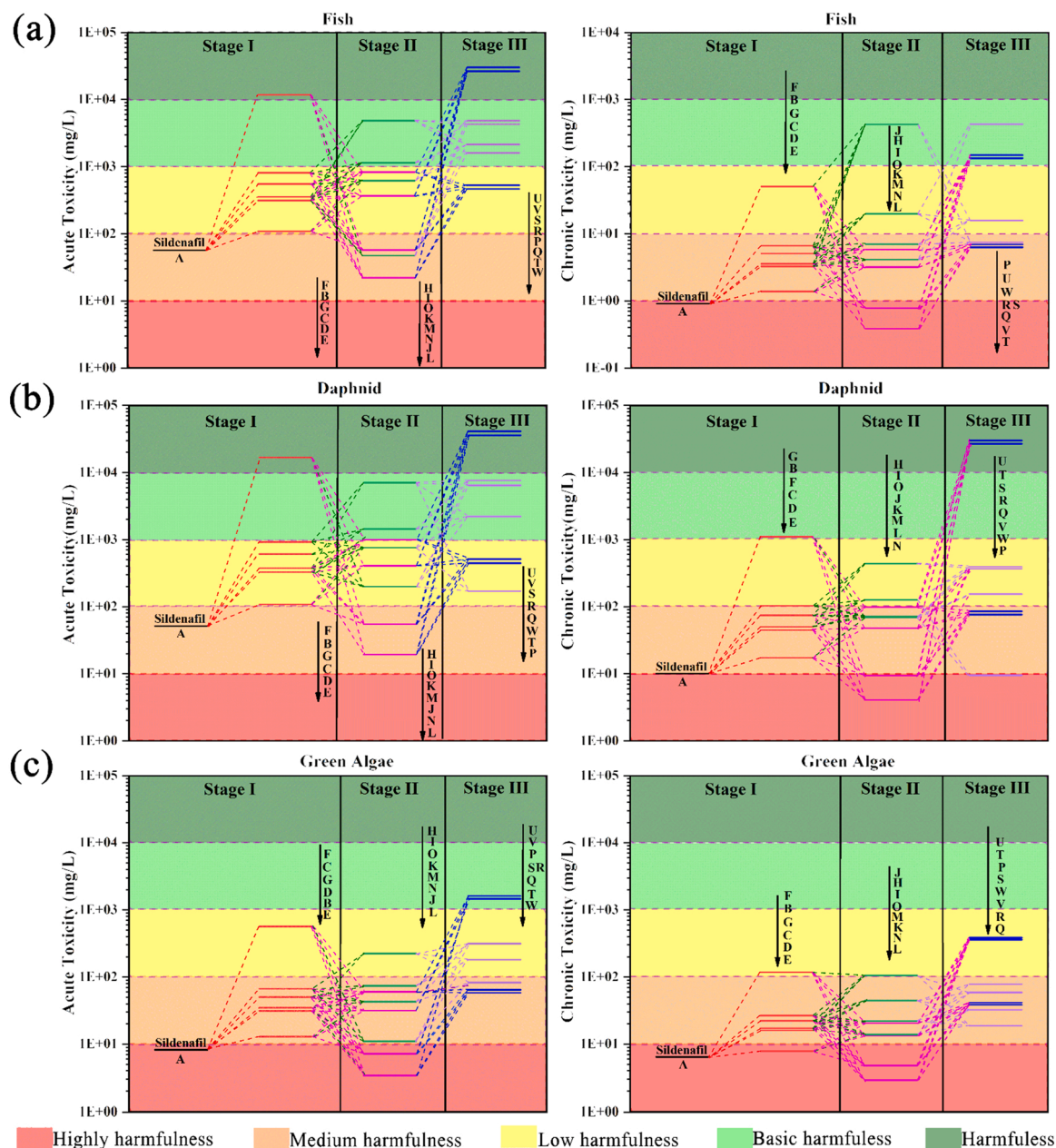
Fig. 10. Prediction of acute toxicity and chronic toxicity for a) fish, b) daphnids, and c) green algae *via* different QSAR models.
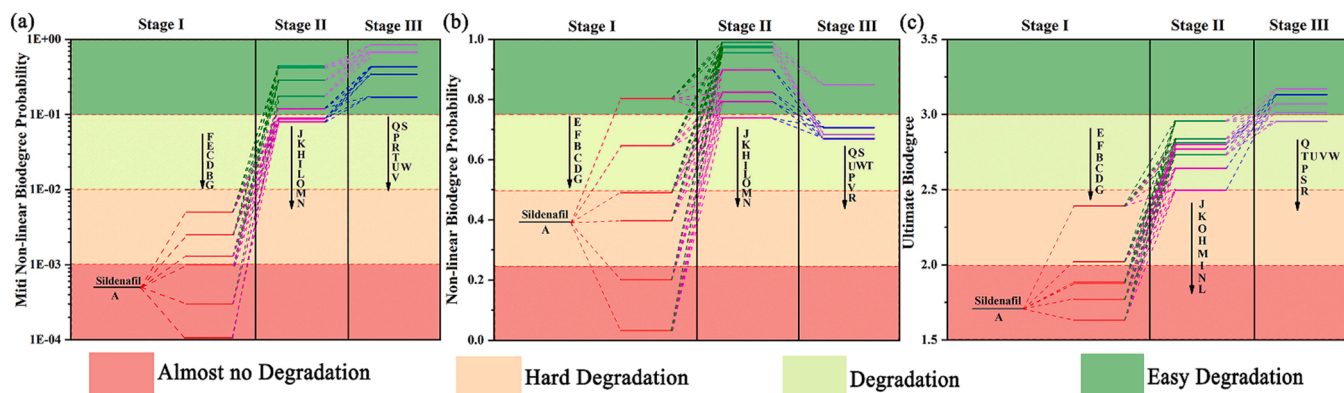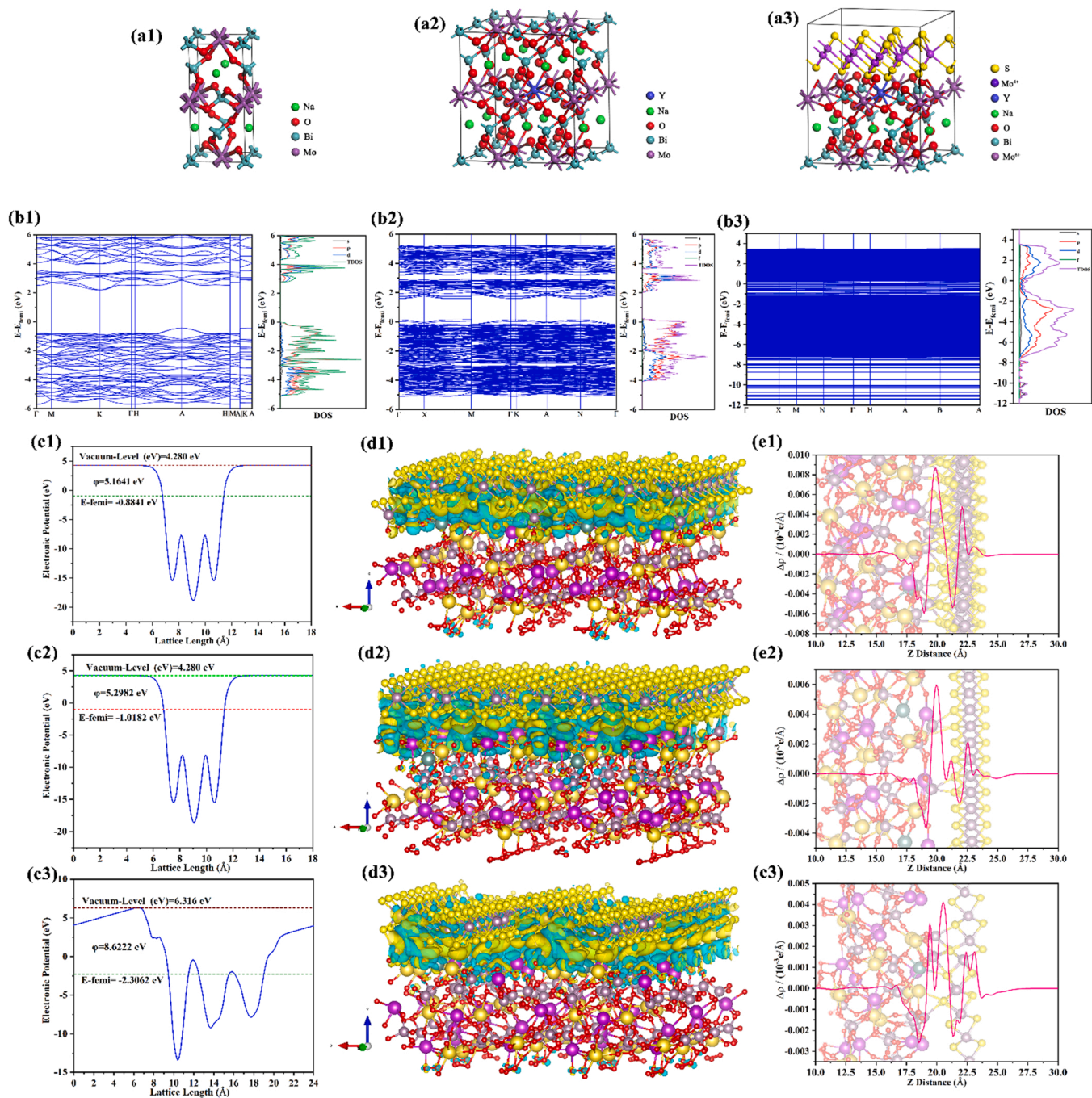

Fig. 11. Prediction of Biodegree Probability for a) MITI Non-liner bio-degree, b) Ultimate bio-degree, and c) Non-linear bio-degree different QSAR model.

Fig. 12. a1-a3) DFT Calculation model for NBMO, 1.5Y-NBMO, and 1T-2H MSQD/1.5Y-NBMO. b1-b3) DFT Calculation of band structure and density of state for NBMO, 1.5Y-NBMO, and 1T-2H MSQD/1.5Y-NBMO. DFT Calculation of c1-c3) work-function, d1-d3) differential charge density and e1-e3) 2D differential charge even distribution curve for 1T MoS$_2$, 2H MoS$_2$ and 1T-2H MSQD/1.5Y-NBMO.

Figs. 12d1–d3 and S20a–b, the work functions φ of the 1T MSQD, 2H MSQD, 1T-2H MSQD, NBMO, and 1.5Y-NBMO were calculated using the GGA-PBE method to be $\varphi = 5.1681$ eV, $\varphi = 5.295$ eV, $\varphi = 5.6402$ eV, $\varphi = 5.1264$ eV, and $\varphi = 8.622$ eV, respectively. The Fermi level of 1T, 2H, 1T-2H, NBMO, and 1.5Y-NBMO were ranked as 1T MSQD (E-femi = −0.8841 eV), 2H MSQD (E-femi = −1.0182 eV), 1T-2H MSQD (E-femi = −1.3342 eV), NBMO (E-femi = −0.9884 eV), and 1.5Y-NBMO (E-femi = −2.3062 eV), respectively. According to the DFT calculation results, a heterostructure formed in 1T MSQD/1.5Y-NBMO and 1T-2H MSQD, and two different types of S-scheme heterojunctions formed in 2H MSQD ($\varphi = 5.295$ eV)/1.5Y-NBMO ($\varphi = 8.622$ eV) and 1T-2H MSQD ($\varphi = 5.6402$ eV)/1.5Y-NBMO ($\varphi = 8.622$ eV). Y^{3+} doping engineering

changes the electronic structure of NBMO, resulting in a decrease in the Fermi energy level (−0.9884 eV to −2.3062 eV) and an increase in the work function (5.1624–8.622 eV), providing optimal conditions for further interfacial polarization. Thus, the DFT calculation results indicated that electrons flow from the surfaces of 1T MSQD and 2H MSQD to that of 1.5Y-NBMO, as well as from the surface of 1T MSQD to that of 2H MSQD, until they both reach the same Fermi energy level. The surfaces of 1T MSQD, 2H MSQD, and 1.5Y-NBMO were charged due to electron transfer; the 1.5Y-NBMO surface was negatively charged, while the 1T MSQD and 2H MSQD surfaces were positively charged, and three internal electric fields were generated at the interface.

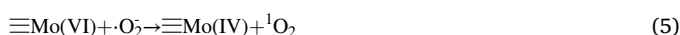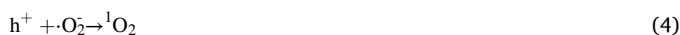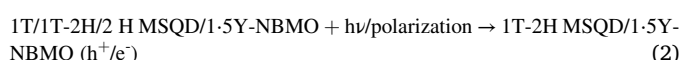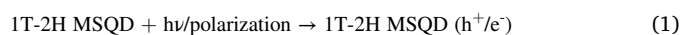To further analyze the charge transfer and separation between the 1T

MSQD/1.5Y-NBMO, 2H MSQD/1.5Y-NBMO, and 1T-2H MSQD/1.5Y-NBMO heterostructure interfaces, the plane-averaged differential charge density along the Z-axis of the heterostructures for the system was calculated theoretically, as shown in Figs. 12d1–d3, e1–e3, and S21d–f. Charge redistribution occurs primarily near the interfaces of 1T, 2H, 1T-2H MSQD, and 1.5Y-NBMO, but the internal charge density inside 1.5Y-NBMO and 1T, 2H, 1T-2H MSQD internal charge density varies very little, indicating the formation of heterojunctions and strong interfacial polarization. The yellow and cyan regions showed charge accumulation and depletion, respectively. Charge accumulation occurred mainly on the 1.5Y-NBMO side, while charge depletion occurred mainly on the 1T, 2H, and 1T-2H MSQD sides. The 1T MSQD/1.5Y-NBMO, 2H MSQD/1.5Y-NBMO, and 1T-2H MSQD/1.5Y-NBMO heterojunction interfaces show that electrons are primarily transferred from 1T MSQD to 2H MSQD, and 1T MSQD or 2H MSQD to 1.5Y-NBMO, whereas the electrons mostly remained on the 1.5Y-NBMO side and holes on the 1T MSQD or 2H MSQD side, which is consistent with the results of the above work function analysis. Moreover, the interfacial polarization caused by the difference in work function induces the piezoelectric effect of the material to appear different, as shown by the 2D differential charge even distribution curve in Figs. 12e1–e3. The peak strength of the charge distribution curve is proportional to the magnitude of the difference in the work function of the two phases of the material; the greater the difference in the work function, the stronger the peak of the charge distribution curve. The 2D differential charge even distribution curve defined the strength of the interface polarization as 1T MSQD (φ = 5.1681 eV)/1.5Y-NBMO (φ = 8.622 eV), 2H MSQD (φ = 5.295 eV)/1.5Y-NBMO (φ = 8.622 eV), and 1T-2H MSQD (φ = 5.6402 eV)/1.5Y-NBMO (φ = 8.622 eV), reflecting the magnitude of the piezoelectric polarization effect. Therefore, two built-in electric fields were created at their interface *via* heterojunction and piezoelectric polarization effects from the surface of 1T MSQD or 2H MSQD to the surface of 1.5Y-NBMO. 2H MSQD and 1T-2H MSQD formed two types of S-scheme heterojunctions and generated a piezoelectric polarization effect with 1.5Y-NBMO. At the same time, the presence of an external electric field in the PEC process, combined with the piezoelectric polarization effect, drives further electron transfer from the electrode material to the cathode, and the simultaneous action of internal and external electric fields accelerates the accumulation of holes in the 1T-2H MSQD/1.5Y-NBMO electrode material, strengthening the hole- and multiradical synergy dominated mechanism of the 1T-2H MSQD/1.5Y-NBMO electrode in the PZ-PEC process and enhancing the PZ-PEC performance of photoelectrodes.

The PZ-PEC device for Sildenafil degradation, shown in Fig. 13a, consists of a visible-light source and a PEC cell; the ions and pollutants migrate between the SSM anode and cathode in the PEC process. Fig. 13b exhibits the various piezoelectric polarization effects of 1T MSQD/1.5Y-NAMO, 2H MSQD/1.5Y-NAMO, and 1T-2H MSQD/1.5Y-NAMO. As shown in Fig. 13c, the above characterization and evaluation revealed the PZ-PEC mechanism of the 1T-2H MSQD/1.5Y-NBMO electrode during the PZ-PEC process. Multiple heterostructures with two types of S-scheme heterojunctions coexisting in 1T-2H MSQD/1.5Y-NBMO electrodes improved the PZ-PEC properties. For 1T-2H MoS$_2$ QDs and 1T MSQD/1.5Y-NAMO heterostructures, the Mo(IV) of 1T MoS$_2$ QDs underwent a charge transfer to 2H MoS$_2$ and 1.5Y-NBMO. The electrons of 2H MoS$_2$ QDs and 1.5Y-NBMO migrated to the SSM anode, then to the SSM cathode, where they reduced O$_2$ to·O$_2^-$, before being oxidized to Mo(VI) by the built-in electric field effect induced by the work function difference, piezoelectric polarization effect, and external bias. The Mo(VI) of 1T MoS$_2$ QDs oxidized·O$_2^-$ to produce ^{1}O$_2$, and photo-excited and piezoelectric polarization-generated holes on the 2H MoS$_2$ QDs and 1.5Y-NBMO valence band oxidized·O$_2^-$ and pollutants to produce ^{1}O$_2$ and intermediates. However, 1.5Y-NBMO could also oxidize OH$^-$ to produce·OH *via* the formation of Bi-S-Mo(IV) and Mo(IV)-S-Mo(VI) electron transfer channels, and H$_2$O$_2$ is then decomposed into undifferentiated aggressive·OH *via* the transitions of Mo(IV) and Mo(VI)
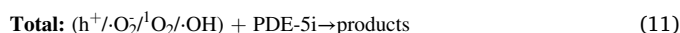
[90,91].

For 2H MSQD/1.5Y-NBMO, the S-scheme heterojunction and piezoelectric polarization effect induced by the work function difference rapidly optimized the recombination of photogenerated electrons and holes with low activity. High-activity photogenerated electrons then effectively migrated to the SSM anode, before moving to the SSM anode to reduce·O$_2^-$ to ^{1}O$_2$. High-activity photogenerated holes rapidly accumulated to effectively oxidize·O$_2^-$, OH$^-$, and pollutants to ^{1}O$_2$,·OH, and intermediates, respectively. The 1T-2H MSQD/1.5Y-NBMO combines the advantages of the 1T-2H MoS$_2$ QDs heterostructure and the 1T-2H MSQD/1.5Y-NBMO S-scheme heterojunction to achieve effective electron transfer and migration as well as the accumulation of holes with high activity. Moreover, the direction of the external bias voltage was the same as that of the built-in electric field on the n-type 1.5Y-NAMO side, which reinforced the built-in electric field of 1T-2H MSQD/1.5Y-NBMO. The multiple heterostructures created by the synergy of piezoelectric polarization and PEC direct oxide pollutants or indirectly produce·O$_2^-$,·OH, and ^{1}O$_2$ to oxide pollutants *via* diversified channels, improving the degradation efficiency of PDE-5i during the PZ-PEC process.

Photoanodes:

$$1T\text{-}2H\ MSQD + h\nu/polarization \rightarrow 1T\text{-}2H\ MSQD\ (h^+/e^-) \qquad (1)$$

$$1T/1T\text{-}2H/2H\ MSQD/1.5Y\text{-}NBMO + h\nu/polarization \rightarrow 1T\text{-}2H\ MSQD/1.5Y\text{-}NBMO\ (h^+/e^-) \qquad (2)$$

$$h^+ + OH^- \rightarrow OH \qquad (3)$$

$$h^+ + \cdot O_2^- \rightarrow {}^1O_2 \qquad (4)$$

$$\equiv Mo(VI) + \cdot O_2^- \rightarrow \equiv Mo(IV) + {}^1O_2 \qquad (5)$$

$$\equiv Mo(IV) + H_2O_2 \rightarrow \equiv Mo(VI) + 2\cdot OH \qquad (6)$$

$$\equiv Mo(VI) + 2\ H_2O_2 \rightarrow 2\cdot O_2^- + 4\ H^+ + \equiv Mo(IV) \qquad (7)$$

Cathode:

$$O_2 + SSM\text{-}Cathode(e^-) \rightarrow \cdot O_2^- \qquad (8)$$

$$\cdot O_2^- + 2\ H^+ + e^- \rightarrow H_2O_2 \qquad (9)$$

$$H_2O_2 + e^- \rightarrow OH^- + \cdot OH \qquad (10)$$

**Total:** $(h^+/\cdot O_2^-/{}^1O_2/\cdot OH) + PDE\text{-}5i \rightarrow products \qquad (11)$

4. Conclusion

In conclusion, interface polarization engineering was used to develop a 1T-2H MSQD/1.5Y-NBMO multi-heterostructure system with two types of S-scheme heterojunctions for piezoelectric-photoelectrocatalysis, as well as a 1T-2H MSQD/1.5Y-NBMO PT-SSM photoelectrode. All characterization and DFT calculations indicated that the doping of heavy rare earth Y^{3+} optimizes the piezoelectric and optoelectronic properties of NaBi(MoO$_4$)$_2$ by optimizing its energy band structure and modifying distinct phase states. MoS$_2$ QDs generate multiple heterostructures and Bi-S-Mo(IV), Mo(IV)-S-Mo(VI) charge transfer channels, which ultimately results in the differential enhancement of the piezoelectric and optoelectronic properties of Y-NaBi(MoO$_4$)$_2$. Among them, the maximum piezoelectric response amplitude enhancement is nearly 12 times. The 1T-2H MSQD/1.5Y-NBMO PT-SSM photoelectrode exhibits remarkable PZ-PEC efficiency for PDE-5i degradation, with kinetic constants approximately 14.60 times that of the NBMO PT-SSM electrode in the PZ-PEC process, 8.86 times that of the 1T MSQD/1.5Y-NBMO PT-SSM electrode in a single PZC process, and 1.95 times that of the 1T-2H MSQD/1.5Y-NBMO PT-SSM electrode in a single PEC process, confirming the synergy between the piezoelectric effect and PEC under optimal conditions. Meanwhile, the QSAR results show that
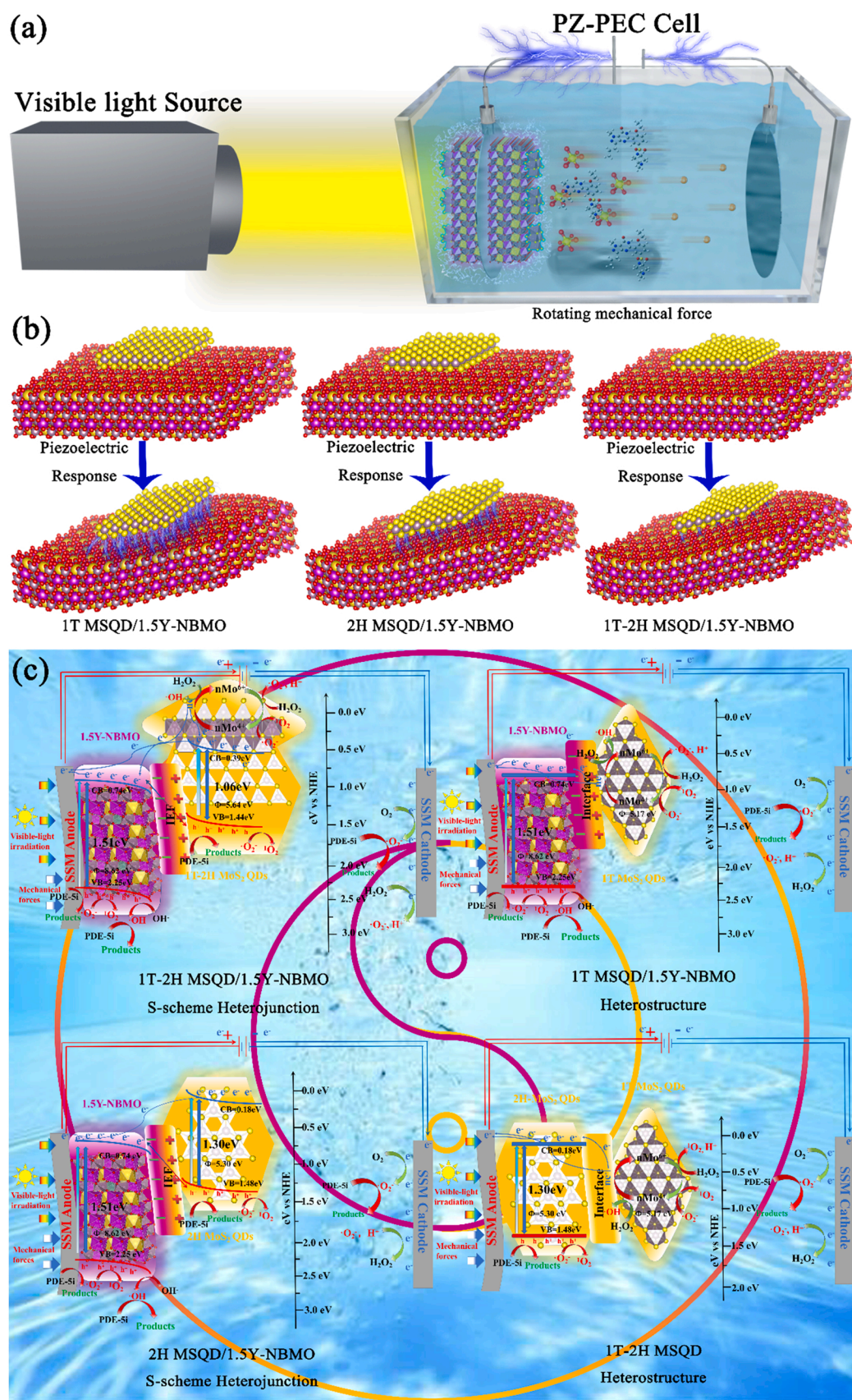
Fig. 13. a) Schematic diagram of the PEC reactive device and process. b) Piezoelectric response diagram of three types of heterostructures. c) PZ-PEC degradation of PDE-5i mechanism for 1T-2H MSQD/1.5Y-NBMO PT-SSM electrode.

the PZ-PEC degradation process considerably decrease the ecological toxicity and improve the biodegradability of Sildenafil products. This work demonstrates a rational approach for synergizing the piezoelectric effect and PEC, and may be applied in the purification of complex ecological risk pollutants.

CRediT authorship contribution statement

Qing-rui Zeng and Zi-ang Jia contributed to overall organizing of all experiments, and writing-original draft preparation. Xu liu and Bo-wen Xiu contributed to calculation, data analysis and visualization. Jin-ping Cheng contributed to methodology, fundation and supervision.

Declaration of Competing Interest

The authors declare that they have no known competing financial interests or personal relationships that could have appeared to influence the work reported in this paper.

Data Availability

The data that has been used is confidential.

Acknowledgments

Appendix A. Supporting information

Supplementary data associated with this article can be found in the online version at doi:10.1016/j.apcatb.2023.122460.

References

[1] Y. Hong, I. Lee, B. Tae, W. Lee, S.-Y. Pan, S.W. Snyder, H. Kim, Contribution of sewage to occurrence of phosphodiesterase-5 inhibitors in natural water, Sci. Rep. 11 (2021) 9470.
[2] K. Hasegawa, O. Suzuki, K. Gonmori, I. Yamagishi, H. Nozawa, K. Watanabe, Simultaneous analysis of sildenafil, vardenafil, tadalafil, and their desalkyl metabolites in human whole blood and urine by isotope dilution LC–MS–MS, Forensic Toxicol. 30 (2012) 25–32.
[3] J.H. Lee, N.S. Kim, K.M. Han, S.H. Kim, S. Cho, W.S. Kim, Monitoring by LC-MS/ MS of 48 compounds of sildenafil, tadalafil, vardenafil and their analogues in illicit health food products in the Korean market advertised as enhancing male sexual performance, Food Addit. Contam. Part A 30 (2013) 1849–1857.
[4] M. Boolell, S. Gepi-Attee, J.C. Gingell, M.J. Allen, Sildenafil, a novel effective oral therapy for male erectile dysfunction, Br. J. Urol. 78 (1996) 257–261.
[5] B.-P. Jiann, Evolution of phosphodiesterase type 5 inhibitors in treatment of erectile dysfunction in Taiwan, Urol. Sci. 27 (2016) 66–70.
[6] Aytaç, Mckinlay Krane, The likely worldwide increase in erectile dysfunction between 1995 and 2025 and some possible policy consequences, BJU Int. 84 (1999) 50–56.
[7] J.-H. Lee, J.-K. Choi, S.-H. Kim, K.-H. Cho, Y.-T. Kim, S.-H. Choi, U.-W. Jung, Association between periodontal flap surgery for periodontitis and vasculogenic erectile dysfunction in Koreans, J. Periodontal Implant Sci. 47 (2017) 96–105.
[8] P. Eichhorn, S. Pérez, J. Aceña, P. Gardinali, J.L. Abad, D. Barceló, Identification of phototransformation products of sildenafil (Viagra) and its N-demethylated human metabolite under simulated sunlight, J. Mass Spectrom. 47 (2012) 701–711.
[9] F. Temussi, M. DellaGreca, P. Pistillo, L. Previtera, A. Zarrelli, E. Criscuolo, M. Lavorgna, C. Russo, M. Isidori, Sildenafil and tadalafil in simulated chlorination conditions: ecotoxity of drugs and their derivatives, Sci. Total Environ. 463–464 (2013) 366–373.
[10] A. Mendoza, J. Aceña, S. Pérez, M. López de Alda, D. Barceló, A. Gil, Y. Valcárcel, Pharmaceuticals and iodinated contrast media in a hospital wastewater: a case study to analyse their presence and characterise their environmental risk and hazard, Environ. Res. 140 (2015) 225–241.
[11] A. Causanilles, E. Emke, P. de Voogt, Determination of phosphodiesterase type V inhibitors in wastewater by direct injection followed by liquid chromatography coupled to tandem mass spectrometry, Sci. Total Environ. 565 (2016) 140–147.
[12] D.R. Baker, B. Kasprzyk-Hordern, Multi-residue analysis of drugs of abuse in wastewater and surface water by solid-phase extraction and liquid

[13] chromatography–positive electrospray ionisation tandem mass spectrometry, J. Chromatogr. A 1218 (2011) 1620–1631.
[13] H. Fr. Schröder, W. Gebhardt, M. Thevis, Anabolic, doping, and lifestyle drugs, and selected metabolites in wastewater—detection, quantification, and behaviour monitored by high-resolution MS and MSnbefore and after sewage treatment, Anal. Bioanal. Chem. 398 (2010) 1207–1229.
[14] M. Papageorgiou, C. Kosma, D. Lambropoulou, Seasonal occurrence, removal, mass loading and environmental risk assessment of 55 pharmaceuticals and personal care products in a municipal wastewater treatment plant in Central Greece, Sci. Total Environ. 543 (2016) 547–569.
[15] D.R. Baker, B. Kasprzyk-Hordern, Spatial and temporal occurrence of pharmaceuticals and illicit drugs in the aqueous environment and during wastewater treatment: New developments, Sci. Total Environ. 454–455 (2013) 442–456.
[16] A. Nieto, M. Peschka, F. Borrull, E. Pocurull, R.M. Marcé, T.P. Knepper, Phosphodiesterase type V inhibitors: occurrence and fate in wastewater and sewage sludge, Water Res. 44 (2010) 1607–1615.
[17] Q. Sun, M. Lv, A. Hu, X. Yang, C.-P. Yu, Seasonal variation in the occurrence and removal of pharmaceuticals and personal care products in a wastewater treatment plant in Xiamen, China, J. Hazard. Mater. 277 (2014) 69–75.
[18] N. Delgado, A. Navarro, D. Marino, G.A. Peñuela, A. Ronco, Removal of pharmaceuticals and personal care products from domestic wastewater using rotating biological contactors, Int. J. Environ. Sci. Technol. 16 (2019) 1–10.
[19] M.G. Abrile, M.M. Ciucio, L.M. Demarchi, V.M. Bono, M.L. Fiasconaro, M. E. Lovato, Degradation and mineralization of the emerging pharmaceutical pollutant sildenafil by ozone and UV radiation using response surface methodology, Environ. Sci. Pollut. Res. 28 (2021) 23868–23886.
[20] L.P. Herbert, D.B. Becker-Krail, W.C. Cory, Persistent phototransformation products of vardenafil (Levitra®) and sildenafil (Viagra®), Chemosphere 134 (2015) 557–562.
[21] G.G. Bessegato, T.T. Guaraldo, J.F. de Brito, M.F. Brugnera, M.V.B. Zanoni, Achievements and trends in photoelectrocatalysis: from environmental to energy applications, Electrocatalysis 6 (2015) 415–441.
[22] P. Lianos, Production of electricity and hydrogen by photocatalytic degradation of organic wastes in a photoelectrochemical cell: The concept of the Photofuelcell: a review of a re-emerging research field, J. Hazard. Mater. 185 (2011) 575–590.
[23] J.C. Cardoso, T.M. Lizier, M.V.B. Zanoni, Highly ordered TiO_2 nanotube arrays and photoelectrocatalytic oxidation of aromatic amine, Appl. Catal. B Environ. 99 (2010) 96–102.
[24] M.F. Brugnera, M. Miyata, G.J. Zocolo, C.Q. Fujimura Leite, M.V. Boldrin Zanoni, A photoelectrocatalytic process that disinfects water contaminated with Mycobacterium kansasii and Mycobacterium avium, Water Res. 47 (2013) 6596–6605.
[25] F.M.M. Paschoal, G. Pepping, M.V.B. Zanoni, M.A. Anderson, Photoelectrocatalytic removal of bromate using Ti/TiO_2 coated as a photocathode, Environ. Sci. Technol. 43 (2009) 7496–7502.
[26] Z.L. Wang, Nanopiezotronics, Adv. Mater. 19 (2007) 889–892.
[27] Z. Liang, C.-F. Yan, S. Rtimi, J. Bandara, Piezoelectric materials for catalytic/ photocatalytic removal of pollutants: Recent advances and outlook, Appl. Catal. B Environ. 241 (2019) 256–269.
[28] G. Nie, L. Xiao, J. Bi, S. Wang, X. Duan, New insight to piezocatalytic peroxymonosulfate activation: the critical role of dissolved oxygen in mediating radical and nonradical pathways, Appl. Catal. B Environ. 315 (2022), 121584.
[29] L. Zhou, S. Dai, S. Xu, Y. She, Y. Li, S. Leveneur, Y. Qin, Piezoelectric effect synergistically enhances the performance of $Ti_{32-oxo-cluster}/BaTiO_3/CuS$ p-n heterojunction photocatalytic degradation of pollutants, Appl. Catal. B Environ. 291 (2021) 120019.
[30] J. Hu, Y. Chen, Y. Zhou, L. Zeng, Y. Huang, S. Lan, M. Zhu, Piezo-enhanced charge carrier separation over plasmonic Au-BiOBr for piezo-photocatalytic carbamazepine removal, Appl. Catal. B Environ. 311 (2022), 121369.
[31] X. Huang, R. Lei, J. Yuan, F. Gao, C. Jiang, W. Feng, J. Zhuang, P. Liu, Insight into the piezo-photo coupling effect of $PbTiO_3/CdS$ composites for piezo-photocatalytic hydrogen production, Appl. Catal. B: Environ. 282 (2021), 119586.
[32] Z. Wang, X. Li, Q. Wei, X. Long, Spectral properties of $Tm^{3+}:NaGd(MoO_4)_2$ crystal, Mater. Res. Bull. 43 (2008) 2961–2965.
[33] Y. Gan, W. Liu, W. Zhang, W. Li, Y. Huang, K. Qiu, Effects of Gd^{3+} codoping on the enhancement of the luminescent properties of a $NaBi(MoO_4)_2:Eu^{3+}$ red-emitting phosphors, J. Alloy. Compd. 784 (2019) 1003–1010.
[34] Y. Li, T. Cao, Z. Mei, X. Li, D. Sun, Separating type I heterojunction of $NaBi$ $(MoO_4)_2/Bi_2MoO_6$ by TiO_2 nanofibers for enhanced visible-photocatalysis, Chem. Phys. 533 (2020), 110696.
[35] A. Hasani, M. Tekalgne, Q.V. Le, H.W. Jang, S.Y. Kim, Two-dimensional materials as catalysts for solar fuels: hydrogen evolution reaction and CO_2 reduction, J. Mater. Chem. A 7 (2019) 430–454.
[36] Q. Yun, Q. Lu, X. Zhang, C. Tan, H. Zhang, Three-dimensional architectures constructed from transition-metal dichalcogenide nanomaterials for electrochemical energy storage and conversion, Angew. Chem. Int. Ed. 57 (2018) 626–646.
[37] G.H. Han, D.L. Duong, D.H. Keum, S.J. Yun, Y.H. Lee, van der waals metallic transition metal dichalcogenides, Chem. Rev. 118 (2018) 6297–6336.
[38] B. Shao, Z. Liu, G. Zeng, Y. Liu, Q. Liang, Q. He, T. Wu, Y. Pan, J. Huang, Z. Peng, S. Luo, C. Liang, X. Liu, S. Tong, J. Liang, Synthesis of 2D/2D CoAl-LDHs/$Ti_3C_2T_x$ Schottky-junction with enhanced interfacial charge transfer and visible-light photocatalytic performance, Appl. Catal. B: Environ. 286 (2021), 119867.

[39] J.M. Wu, W.E. Chang, Y.T. Chang, C.-K. Chang, Piezo-catalytic effect on the enhancement of the ultra-high degradation activity in the dark by single- and few-layers MoS$_2$ nanoflowers, Adv. Mater. 28 (2016) 3718–3725.

[40] L. Pan, S. Sun, Y. Chen, P. Wang, J. Wang, X. Zhang, J.-J. Zou, Z.L. Wang, Advances in piezo-phototronic effect enhanced photocatalysis and photoelectrocatalysis, Adv. Energy Mater. 10 (2020) 2000214.

[41] P. Lin, L. Zhu, D. Li, L. Xu, C. Pan, Z. Wang, Piezo-phototronic effect for enhanced flexible MoS$_2$/WSe$_2$ van der waals photodiodes, Adv. Funct. Mater. 28 (2018) 1802849.

[42] C. Zhu, P. Liu, B. Niu, Y. Liu, W. Xin, W. Chen, X.-Y. Kong, Z. Zhang, L. Jiang, L. Wen, Metallic two-dimensional MoS$_2$ composites as high-performance osmotic energy conversion membranes, J. Am. Chem. Soc. 143 (2021) 1932–1940.

[43] E.E. Benson, H. Zhang, S.A. Schuman, S.U. Nanayakkara, N.D. Bronstein, S. Ferrere, J.L. Blackburn, E.M. Miller, Balancing the hydrogen evolution reaction, surface energetics, and stability of metallic mos2 nanosheets via covalent functionalization, J. Am. Chem. Soc. 140 (2018) 441–450.

[44] X. Zhao, S. Ning, W. Fu, S.J. Pennycook, K.P. Loh, Differentiating polymorphs in molybdenum disulfide via electron microscopy, Adv. Mater. 30 (2018) 1802397.

[45] X. Hu, X. Zeng, Y. Liu, J. Lu, S. Yuan, Y. Yin, J. Hu, D.T. McCarthy, X. Zhang, Nano-layer based 1T-rich MoS$_2$/g-C$_3$N$_4$ co-catalyst system for enhanced photocatalytic and photoelectrochemical activity, Appl. Catal. B Environ. 268 (2020), 118466.

[46] D. Voiry, R. Fullon, J. Yang, C. de Carvalho Castro e Silva, R. Kappera, I. Bozkurt, D. Kaplan, M.J. Lagos, P.E. Batson, G. Gupta, Aditya D. Mohite, L. Dong, D. Er, V. B. Shenoy, T. Asefa, M. Chhowalla, The role of electronic coupling between substrate and 2D MoS$_2$ nanosheets in electrocatalytic production of hydrogen, Nat. Mater. 15 (2016) 1003–1009.

[47] Y. Liu, Y. Li, F. Peng, Y. Lin, S. Yang, S. Zhang, H. Wang, Y. Cao, H. Yu, 2H- and 1T-mixed phase few-layer MoS$_2$ as a superior to Pt co-catalyst coated on TiO$_2$ nanorod arrays for photocatalytic hydrogen evolution, Appl. Catal.: B: Environ. 241 (2019) 236–245.

[48] X. Li, X. Lv, N. Li, J. Wu, Y.-Z. Zheng, X. Tao, One-step hydrothermal synthesis of high-percentage 1T-phase MoS$_2$ quantum dots for remarkably enhanced visible-light-driven photocatalytic H$_2$ evolution, Appl. Catal. B Environ. 243 (2019) 76–85.

[49] A. Okemoto, K. Kishishita, S. Maeda, S. Gohda, M. Misaki, Y. Koshiba, K. Ishida, T. Horie, K. Taniya, Y. Ichihashi, S. Nishiyama, Application of picene thin-film semiconductor as a photocatalyst for photocatalytic hydrogen formation from water, Appl. Catal.: B: Environ. 192 (2016) 88–92.

[50] L. Lin, T. Hisatomi, S. Chen, T. Takata, K. Domen, Visible-light-driven photocatalytic water splitting: recent progress and challenges, Trends Chem. 2 (2020) 813–824.

[51] J.M. Wu, Y.-G. Sun, W.-E. Chang, J.-T. Lee, Piezoelectricity induced water splitting and formation of hydroxyl radical from active edge sites of MoS$_2$ nanoflowers, Nano Energy 46 (2018) 372–382.

[52] M.-H. Wu, J.-T. Lee, Y.J. Chung, M. Srinivaas, J.-M. Wu, Ultrahigh efficient degradation activity of single- and few-layered MoSe$_2$ nanoflowers in dark by piezo-catalyst effect, Nano Energy 40 (2017) 369–375.

[53] H.-Y. Lin, K.T. Le, P.-H. Chen, J.M. Wu, Systematic investigation of the piezocatalysis–adsorption duality of polymorphic MoS$_2$ nanoflowers, Appl. Catal. B Environ. 317 (2022), 121717.

[54] Y.H. Wen, L. Shao, P.C. Zhao, B.Y. Wang, G.P. Cao, Y.S. Yang, Carbon coated stainless steel mesh as a low-cost and corrosion-resistant current collector for aqueous rechargeable batteries, J. Mater. Chem. A 5 (2017) 15752–15758.

[55] A. Yavuz, K. Kaplan, M. Bedir, Metal oxides composite electrode with high areal capacitance formed by thermal oxidation of stainless steel mesh, J. Solid State Electrochem. 26 (2022) 1333–1347.

[56] X. Ying, D. Shen, M. Wang, H. Feng, Y. Gu, W. Chen, Titanium dioxide thin film-modified stainless steel mesh for enhanced current-generation in microbial fuel cells, Chem. Eng. J. 333 (2018) 260–267.

[57] Q. Tan, R. Xiao, X. Yao, T. Xiong, J. Li, Y.-w Hu, Y. Huang, M.S. Balogun, Non-oxygen anion-regulated in situ cobalt based heterojunctions for active alkaline hydrogen evolution catalysis, Chem. Eng. J. 433 (2022), 133514.

[58] Y.-J. Shih, Z.-L. Wu, C.-Y. Lin, Y.-H. Huang, C.-P. Huang, Manipulating the crystalline morphology and facet orientation of copper and copper-palladium nanocatalysts supported on stainless steel mesh with the aid of cationic surfactant to improve the electrochemical reduction of nitrate and N$_2$ selectivity, Appl. Catal. B Environ. 273 (2020), 119053.

[59] M. Yao, N. Wang, W. Hu, S. Komarneni, Novel hydrothermal electrodeposition to fabricate mesoporous film of Ni$_{0.8}$Fe$_{0.2}$ nanosheets for high performance oxygen evolution reaction, Appl. Catal. B Environ. 233 (2018) 226–233.

[60] M.B. Sassin, C.N. Chervin, D.R. Rolison, J.W. Long, Redox deposition of nanoscale metal oxides on carbon for next-generation electrochemical capacitors, Acc. Chem. Res. 46 (2013) 1062–1074.

[61] R. Cao, H. Huang, N. Tian, Y. Zhang, Y. Guo, T. Zhang, Novel Y doped Bi$_2$WO$_6$ photocatalyst: Hydrothermal fabrication, characterization and enhanced visible-light-driven photocatalytic activity for Rhodamine B degradation and photocurrent generation, Mater. Charact. 101 (2015) 166–172.

[62] Y. Tian, L. Zhang, J. Zhang, A superior visible light-driven photocatalyst: europium-doped bismuth tungstate hierarchical microspheres, J. Alloy. Compd. 537 (2012) 24–28.

[63] H. Huang, H. Qi, Y. He, N. Tian, Y. Zhang, Enhanced photocatalytic activity of Eu^{3+}- and Gd^{3+}-doped BiPO$_4$, J. Mater. Res. 28 (2013) 2977–2984.

[64] W. Luo, F. Li, Q. Li, X. Wang, W. Yang, L. Zhou, L. Mai, Heterostructured Bi$_2$S$_3$–Bi$_2$O$_3$ nanosheets with a built-in electric field for improved sodium storage, ACS Appl. Mater. Interfaces 10 (2018) 7201–7207.

[65] X.-H. Zhang, N. Li, J. Wu, Y.-Z. Zheng, X. Tao, Defect-rich O-incorporated 1T-MoS$_2$ nanosheets for remarkably enhanced visible-light H$_2$ evolution over CdS: the impact of enriched defects, Appl. Catal. B Environ. 229 (2018) 227–236.

[66] B. Li, L. Jiang, X. Li, P. Ran, P. Zuo, A. Wang, L. Qu, Y. Zhao, Z. Cheng, Y. Lu, Preparation of monolayer MoS$_2$ quantum dots using temporally shaped femtosecond laser ablation of bulk MoS$_2$ targets in liquid, Sci. Rep. 7 (2017) 11182.

[67] Z. Lei, J. Zhan, L. Tang, Y. Zhang, Y. Wang, Recent development of metallic (1T) phase of molybdenum disulfide for energy conversion and storage, Adv. Energy Mater. 8 (2018) 1703482.

[68] G. Eda, H. Yamaguchi, D. Voiry, T. Fujita, M. Chen, M. Chhowalla, Photoluminescence from chemically exfoliated MoS$_2$, Nano Lett. 11 (2011) 5111–5116.

[69] C. Lee, H. Yan, L.E. Brus, T.F. Heinz, J. Hone, S. Ryu, Anomalous lattice vibrations of single- and few-layer MoS$_2$, ACS Nano 4 (2010) 2695–2700.

[70] É. Blanco, P. Afanasiev, G. Berhault, D. Uzio, S. Loridant, Resonance Raman spectroscopy as a probe of the crystallite size of MoS$_2$ nanoparticles, Comptes Rendus Chim. 19 (2016) 1310–1314.

[71] D. Kong, H. Wang, J.J. Cha, M. Pasta, K.J. Koski, J. Yao, Y. Cui, Synthesis of MoS$_2$ and MoSe$_2$ films with vertically aligned layers, Nano Lett. 13 (2013) 1341–1347.

[72] S. Jiménez Sandoval, D. Yang, R.F. Frindt, J.C. Irwin, Raman study and lattice dynamics of single molecular layers of MoS$_2$, Phys. Rev. B 44 (1991) 3955–3962.

[73] Q. Ding, F. Meng, C.R. English, M. Cabán-Acevedo, M.J. Shearer, D. Liang, A. S. Daniel, R.J. Hamers, S. Jin, Efficient photoelectrochemical hydrogen generation using heterostructures of Si and chemically exfoliated metallic MoS$_2$, J. Am. Chem. Soc. 136 (2014) 8504–8507.

[74] X. Fan, P. Xu, D. Zhou, Y. Sun, Y.C. Li, M.A.T. Nguyen, M. Terrones, T.E. Mallouk, Fast and efficient preparation of exfoliated 2H MoS$_2$ nanosheets by sonication-assisted lithium intercalation and infrared laser-induced 1T to 2H phase reversion, Nano Lett. 15 (2015) 5956–5960.

[75] J.V. Silveira, J.A. Batista, G.D. Saraiva, J. Mendes Filho, A.G. Souza Filho, S. Hu, X. Wang, Temperature dependent behavior of single walled MoO$_3$ nanotubes: a Raman spectroscopy study, Vib. Spectrosc. 54 (2010) 179–183.

[76] M. Dieterle, G. Mestl, Raman spectroscopy of molybdenum oxides Part II. Resonance Raman spectroscopic characterization of the molybdenum oxides Mo$_4$O$_{11}$ and MoO$_2$, Phys. Chem. Chem. Phys. 4 (2002) 822–826.

[77] M.A. Lukowski, A.S. Daniel, F. Meng, A. Forticaux, L. Li, S. Jin, Enhanced hydrogen evolution catalysis from chemically exfoliated metallic MoS$_2$ nanosheets, J. Am. Chem. Soc. 135 (2013) 10274–10277.

[78] W. Li, Y. Shen, X. Xiao, C. An, G. Wei, Y. Wang, J. Wang, Y. Wu, C. An, Simple Te-thermal converting 2H to 1T@2H MoS2 homojunctions with enhanced supercapacitor performance, ACS Appl. Energy Mater. 2 (2019) 8337–8344.

[79] L. Zhuang, L. Ge, Y. Yang, M. Li, Y. Jia, X. Yao, Z. Zhu, Ultrathin iron-cobalt oxide nanosheets with abundant oxygen vacancies for the oxygen evolution reaction, Adv. Mater. 29 (2017) 1606793.

[80] S. Heo, S.K. Sharma, S. Lee, Y. Lee, C. Kim, B. Lee, H. Lee, D.Y. Kim, Effects of Y contents on surface, structural, optical, and electrical properties for Y-doped ZnO thin films, Thin Solid Films 558 (2014) 27–30.

[81] W.-T. Tsai, C.-W. Lai, T.-Y. Su, Adsorption of bisphenol-A from aqueous solution onto minerals and carbon adsorbents, J. Hazard. Mater. 134 (2006) 169–175.

[82] P. Chen, L. Blaney, G. Cagnetta, J. Huang, B. Wang, Y. Wang, S. Deng, G. Yu, Degradation of ofloxacin by perylene diimide supramolecular nanofiber sunlight-driven photocatalysis, Environ. Sci. Technol. 53 (2019) 1564–1575.

[83] F. Wang, Y. Feng, P. Chen, Y. Wang, Y. Su, Q. Zhang, Y. Zeng, Z. Xie, H. Liu, Y. Liu, W. Lv, G. Liu, Photocatalytic degradation of fluoroquinolone antibiotics using ordered mesoporous g-C$_3$N$_4$ under simulated sunlight irradiation: kinetics, mechanism, and antibacterial activity elimination, Appl. Catal. B Environ. 227 (2018) 114–122.

[84] F. Qin, Y. Peng, G. Song, Q. Fang, R. Wang, C. Zhang, G. Zeng, D. Huang, C. Lai, Y. Zhou, X. Tan, M. Cheng, S. Liu, Degradation of sulfamethazine by biochar-supported bimetallic oxide/persulfate system in natural water: performance and reaction mechanism, J. Hazard. Mater. 398 (2020), 122816.

[85] C. Zhang, D. Qin, Y. Zhou, F. Qin, H. Wang, W. Wang, Y. Yang, G. Zeng, Dual optimization approach to Mo single atom dispersed g-C$_3$N$_4$ photocatalyst: morphology and defect evolution, Appl. Catal. B Environ. 303 (2022) 120904.

[86] W. Yang, R.G. Parr, Hardness, softness, and the fukui function in the electronic theory of metals and catalysis, Proc. Natl. Acad. Sci. 82 (1985) 6723–6726.

[87] B. Shao, X. Liu, Z. Liu, G. Zeng, W. Zhang, Q. Liang, Y. Liu, Q. He, X. Yuan, D. Wang, S. Luo, S. Gong, Synthesis and characterization of 2D/0D g-C$_3$N$_4$/CdS-nitrogen doped hollow carbon spheres (NHCs) composites with enhanced visible light photodegradation activity for antibiotic, Chem. Eng. J. 374 (2019) 479–493.

[88] H. Guo, H.-Y. Niu, C. Liang, C.-G. Niu, D.-W. Huang, L. Zhang, N. Tang, Y. Yang, C.-Y. Feng, G.-M. Zeng, Insight into the energy band alignment of magnetically separable Ag$_2$O/ZnFe$_2$O$_4$ p-n heterostructure with rapid charge transfer assisted visible light photocatalysis, J. Catal. 370 (2019) 289–303.

[89] W. Wang, Q. Niu, G. Zeng, C. Zhang, D. Huang, B. Shao, C. Zhou, Y. Yang, Y. Liu, H. Guo, W. Xiong, L. Lei, S. Liu, H. Yi, S. Chen, X. Tang, 1D porous tubular g-C$_3$N$_4$ capture black phosphorus quantum dots as 1D/0D metal-free photocatalysts for oxytetracycline hydrochloride degradation and hexavalent chromium reduction, Appl. Catal. B Environ. 273 (2020), 119051.

[90] Q. Yan, C. Lian, K. Huang, L. Liang, H. Yu, P. Yin, J. Zhang, M. Xing, Constructing an acidic microenvironment by MoS$_2$ in heterogeneous fenton reaction for pollutant control, Angew. Chem. Int. Ed. 60 (2021) 17155–17163.

[91] X. Bai, X. Wang, T. Jia, L. Guo, D. Hao, Z. Zhang, L. Wu, X. Zhang, H. Yang, Y. Gong, J. Li, H. Li, Efficient degradation of PPCPs by Mo$_{1−x}$S$_{2−y}$ with S vacancy at phase-junction: promoted by innergenerate-H$_2$O$_2$, Appl. Catal. B Environ. 310 (2022), 121302.